Measuring charge carrier and structural photodynamics at solar energy material surfaces using transient extreme ultraviolet reflection spectroscopy

Thesis by
Jonathan Malte Zschiegner Michelsen

In Partial Fulfillment of the Requirements for the
Degree of
Doctor of Philosophy

CALIFORNIA INSTITUTE OF TECHNOLOGY
Pasadena, California

2024
Defended October 2, 2023

Jonathan Malte Zschiegner Michelsen
ORCID: 0000-0002-7420-5610

ACKNOWLEDGEMENTS

ABSTRACT

Electronic and vibrational degrees of freedom, and their interactions, control the chemical and physical properties of solids. Core-level spectroscopies, such as transient extreme ultraviolet (XUV) spectroscopy, provide detailed information on the electronic structure and local coordination environment of a material. In this work, we employ transient XUV reflection spectroscopy to measure surface carrier and structural dynamics in solar energy materials. To interpret experimental spectra, excited state valence effects are incorporated into the OCEAN code (Obtaining core excitations from ab initio electronic structure and the NIST Bethe-Salpeter equation solver). The modeling of core-level spectra from first principles enables the extraction of carrier kinetics via the robust assignment of spectral features. Moreover, this thesis explores experimental and theoretical methods for understanding carrier-structural coupling in solids relevant to solar energy applications.

Specifically, we explore the chemical and physical information contained in core-level spectra for various solar energy material systems and present guiding principles for designing a core-level electronic spectroscopy experiments to determine photoexcited carrier and structural dynamics. We report on experimental measurements of ultrafast surface carrier and structural dynamics in photocathodes zinc telluride (ZnTe) and copper iron oxide ($CuFeO_2$). Further, complementary excited state theory is presented to extract excited state valence dynamics from experimental core-level spectra based on ground state implementations of the Bethe-Salpeter equation.

PUBLISHED CONTENT AND CONTRIBUTIONS

(1) Liu, H.; Klein, I. M.; Michelsen, J. M.; Cushing, S. K. Element-Specific Electronic and Structural Dynamics using Transient XUV and Soft X-ray Spectroscopy. *Chem* **2021**, *7*, 2569–2584, DOI: `10.1016/j.chempr.2021.09.005`,
J.M.M. participated in the manuscript conception and writing.

(2) Liu, H.; Michelsen, J. M.; Mendes, J. L.; Klein, I. M.; Bauers, S. R.; Evans, J. M.; Zakutayev, A.; Cushing, S. K. Measuring Photoexcited Electron and Hole Dynamics in ZnTe and Modeling Excited State Core-Valence Effects in Transient Extreme Ultraviolet Reflection Spectroscopy. *The Journal of Physical Chemistry Letters* **2023**, *14*, 2106–2111, DOI: `10.1021/acs.jpclett.2c03894`,
J.M.M. participated in the conception of the project, participated in the construction of experimental apparatus, measured experimental optical and XUV spectra, participated in data analysis, calculated momentum-resolved theoretical spectra, and participated in the writing of the manuscript.

TABLE OF CONTENTS

LIST OF ILLUSTRATIONS

Chapter 1

INTRODUCTION

Charge carriers and lattice vibrations control the dynamic behavior of solids. In semiconducting solids, the absorption of photons drives electronic transitions across an energy region without electronic states (termed the band gap)—generating photoexcited electrons and holes in the conduction and valence bands that follow an initial non-equilibrium statistical distribution. Carrier-phonon interactions, the coupling between electronic and vibrational degrees of freedom, cause the initial non-equilibrium carrier distribution to relax towards the equilibrium Fermi-Dirac carrier distribution. These carrier-phonon interactions describe the effect of changing lattice positions on the energy of the charge carrier.[1]

1.1 Electronic spectroscopy

Since the initial photogeneration of charge carriers and subsequent carrier-phonon interactions occur on ultrafast timescales (sub-femtosecond to picosecond), ultrafast methods are required that resolve the coupled carrier-structural dynamics that steer material behavior.[2] Ultrafast electronic spectroscopy is a set of techniques capable of resolving ultrafast changes to the electronic structure of matter. By probing the light-matter interactions using photons at energies similar to the electronic states of interest, a material's ground state electronic structure and its dynamical evolution can be measured.[3, 4]

The interaction between light and matter is dictated by the coupling between the light's electromagnetic field and the material's quantum states of matter. The light's electromagnetic field can be described as an oscillatory plane wave that propagates in the z-direction. The electric field component of this wave is written as a sinusoidal wave with an amplitude E_0, frequency ω, and wavenumber k, propagating in the coordinates of space z and time t.

$$\tilde{E} = E_0 e^{i(kz - \omega t)} \tag{1.1}$$

The wavenumber describes the spatial frequency of the electromagnetic field, determining the light's wavelength λ, phase velocity v, and index of refraction n according to equations 1.2.[5]

$$\lambda = \frac{2\pi}{k}, v = \frac{\omega}{k}, n = \frac{ck}{\omega} \tag{1.2}$$

Commonly used to describe how an oscillating electromagnetic field is modified when propagating through a given material, the complex index of refraction describes changes to the electromagnetic field's intensity and phase. By formulating the wavenumber as a complex quantity, the intensity and phase contributions become directly apparent. The complex wavenumber $\tilde{k}$ consists of the real wavenumber k, in addition to the imaginary component κ.[5]

$$\tilde{k} = k + i\kappa \tag{1.3}$$

When incorporated into the plane wave equation, the real wavenumber k remains responsible for the spatial frequency, while the imaginary component of the wavenumber generally results in an exponential decay of the electric field's intensity as the light travels through the material (i.e. absorption). For most materials measured by electronic spectroscopies, the light's magnetic field strength and material's magnetic permeability are sufficiently low for magnetic effects to be negligible.

$$\tilde{E} = E_0 e^{i(\tilde{k}z - \omega t)} = E_0 e^{-\kappa z} e^{i(kz - \omega t)} \tag{1.4}$$

Since the observed intensity is the square of the electric field, the absorption coefficient α is defined based on the imaginary component of the complex wavenumber.

$$\alpha = 2\text{Im}(\tilde{k}) = 2\kappa \tag{1.5}$$

Connecting this propagating wave to the medium's underlying electric and magnetic properties, the complex wavenumber is related to the light's frequency ω and the material's complex electric permittivity $\tilde{\epsilon}$ and magnetic permeability μ.

$$\tilde{k} \equiv \omega \sqrt{\tilde{\epsilon}\mu} \tag{1.6}$$

The electric permittivity, also known as the dielectric function due to its strong frequency dependence, is similarly complex-valued to capture intensity and phase changes.[6]

$$\tilde{\epsilon} = \epsilon' + i\epsilon'' \tag{1.7}$$

Specifically, the real permittivity ϵ' corresponds to changes in phase, while the imaginary permittivity ϵ'' generally causes a decrease in electric field intensity (absorption). The real and imaginary components of the electric permittivity can be related using the Kramers-Kronig relations. This dielectric function is not directly measurable, but can be extracted from experimental observables of the material's polarization response to an external electric field.[6]

To understand the material's macroscopic response when subjected to an external electric field, the electric susceptibility quantifies the induced electric polarization in a given linear dielectric material (an electrical insulator that can acquire an electric dipole moment). This electric susceptibility $\tilde{\chi}$ is defined as the dimensionless constant relating the material's polarization $\tilde{P}$ response to the applied external electric field $\tilde{E}$.[5]

$$\tilde{P}(\omega) = \epsilon_0 \tilde{\chi}(\omega) \tilde{E}(\omega) \tag{1.8}$$

The electric susceptibility $\tilde{\chi}$ is directly related to the the previously discussed electric permittivity $\tilde{\epsilon}$.

$$\tilde{\epsilon}(\omega) \equiv \epsilon_0 (1 + \tilde{\chi}(\omega)) \tag{1.9}$$

In solids, the electric displacement field is used to describe free charge in addition to the accumulation of bound charges (described by the polarization $\tilde{P}$).

Here, the external electric field $\tilde{E}$ leads to the electric displacement field $\tilde{D}$, which includes the combined effects of the material's polarization and the electromagnetic field. Notably, the displacement field $\tilde{D}$ is again a complex quantity since the material response can be in- or out-of-phase with the complex electric field $\tilde{E}$.[5]

$$\tilde{D}(\omega) = \epsilon_0 \tilde{E}(\omega) + \tilde{P}(\omega) = \epsilon_0 \tilde{E}(\omega) + \epsilon_0 \tilde{\chi}(\omega) \tilde{E}(\omega) = \epsilon_0 (1 + \tilde{\chi}(\omega)) \tilde{E}(\omega) = \tilde{\epsilon}(\omega) \tilde{E}(\omega) \tag{1.10}$$

Experimentally, this electric response of the material to the external electric field can understood by measuring the intensity of the absorbed and/or reflected light. The frequency-dependent reflectance $R(\omega)$ of the material is defined as the ratio of the incident and reflected intensity, which corresponds to the moduli of the incident and reflected complex electric fields.[6]

$$R(\omega) \equiv \frac{I_r(\omega)}{I_i(\omega)} = \frac{E_r^*(\omega)E_r(\omega)}{E_i^*(\omega)E_i(\omega)} \tag{1.11}$$

Through the Fresnel equations describing transmission and reflection of electromagnetic waves, the experimentally-measured reflectance can be related to the underlying refractive index, and thus the material's microscopic electric permittivity by the relation: $\tilde{n} = \sqrt{\tilde{\epsilon}} = \sqrt{\epsilon' + i\epsilon''}$.[6] For s-polarized light, the measured reflection signal at the vacuum-material interface is a function of the material's refractive index $\tilde{n}$ and incident angle θ.[7]

$$R_s(\omega) = \left| \frac{\cos\theta - \sqrt{\tilde{n}^2 - \sin^2\theta}}{\cos\theta + \sqrt{\tilde{n}^2 - \sin^2\theta}} \right|^2 \tag{1.12}$$

To capture the dynamic evolution of the material's quantum states, transient reflection or absorption techniques rely on using a sequence of two light pulses to create an excited electronic state and subsequently probe how this excited state progresses over time. (Due to this time-delayed sequence of excitation and measurement pulses, the technique is commonly referred to as "pump-probe" spectroscopy.) The measured transient absorption or reflection signal originates from the material's third-order non-linear susceptibility. In addition to creating purely electronic states, the pump pulse can impulsively excite coherent vibrational modes, or phonons, if the optical pulse is short compared to the lattice vibration frequency.[8] Thus, transient absorption/reflection techniques provide rich information not only on ultrafast electronic states, but also on coupled carrier-phonon dynamics.

In a reflection geometry, both the absorptive and refractive components of the refractive index (and therefore the complex electric permittivity) have been shown to contribute to the observed specotroscopic signal.[9] By sweeping the incident angle of the experimental geometry relative to an interface θ, the full complex permittivity can hereby be extracted.[6]

1.2 Core-level electronic spectroscopy

Core-level electronic spectroscopy involves the excitation of core-level electrons to valence and continuum states, providing advantages such as carrier- and element-specificity. By exciting a core-level electron to the valence states, these methods can probe valence charge carrier (electrons and holes) and structural dynamics using a well-defined initial state. The initial core states offer element-specificity

by energetically separating core-valence transitions for different elements. In the electric dipole limit $\hat{e} \cdot r$, the intensity of absorbed X-ray photons I depends on the dipole operator acting between the final and initial eigenstates Φ_f and Φ_i.[10]

$$I \sim |\langle \Phi_f | \hat{e} \cdot r | \Phi_i \rangle|^2 \delta(E_f - E_i - \hbar\omega) \tag{1.13}$$

For energy conservation, the incident photon energy $\hbar\omega$ of frequency ω must equal the difference of the eigenstate energies, $E_f - E_i$.

Core-level techniques are widely used due to their sensitivity to the oxidation state and local coordination chemistry. With the availability of increasingly bright sources at high repetition rates (khz-MHz), X-ray experiments have become widely available to scientific fields spanning photochemistry, strong-field physics, and structural biology[11, 12]. In this work, we focus on transient table-top core-level spectroscopies in the lower-energy extreme ultraviolet (XUV) and soft X-ray (SXR) regimes, which offer the additional advantage of being sensitive to surface-level carrier and phonon dynamics (~nm) due to their photons' low penetration depth in solids. Together with an optical pump that photogenerates excited charge carriers, the core-level probe is used to measure the coupled carrier-phonon dynamics in photoactive solids.

1.3 Thesis overview

This thesis explores ultrafast carrier-structural dynamics in solids through experimental transient XUV reflection spectroscopy and complementary ab initio theory. Chapter 2 introduces electronic and core-level spectroscopies for understanding coupled charge carrier-structural dynamics in photoactive materials. Guiding principles are proposed for planning core-level spectroscopy experiments to extract fundamental charge carrier and structural dynamics. The discussion focuses on using core-level probes in the lower-energy XUV and SXR regimes to probe valence carrier and indirect structural dynamics. These core-level transitions feature enhanced sensitivity to valence carrier dynamics compared to higher-energy X-rays that excel at measuring structural dynamics. In Chapter 3, we report measuring carrier-structural surface dynamics in the photocathode zinc telluride (ZnTe). We separately measure non-equilibrium photoexcited electron and hole relaxation dynamics and observe many-body effects including band gap renormalization and coherent phonon oscillations. Carrier dynamics are successfully extracted by robustly assigning excited state spectral features using the Bethe-Salpeter equation. Chapter 4 discusses polaron formation, a form of ultrafast charge carrier self-trapping that severely reduces carrier mobilities in a range of materials. In the transition metal photocathode cop-

per iron oxide ($CuFeO_2$), we measure electronic and structural signatures of small polaron formation and subsequent polaron delocalization.

References

(1) Emin, D., *Polarons*, 1st ed.; Cambridge University Press: 2012.

(2) Hase, M.; Kitajima, M.; Constantinescu, A. M.; Petek, H. The Birth of a Quasiparticle in Silicon Observed in Time–Frequency Space. *Nature* **2003**, *426*, 51–54, DOI: 10.1038/nature02044.

(3) Othonos, A. Probing Ultrafast Carrier and Phonon Dynamics in Semiconductors. *Journal of Applied Physics* **1998**, *83*, 1789–1830, DOI: 10.1063/1.367411.

(4) Fleming, G. R. Subpicosecond Spectroscopy. *Annual Review of Physical Chemistry* **1986**, *37*, 81–104, DOI: 10.1146/annurev.pc.37.100186.000501.

(5) Griffiths, D. J., *Introduction to Electrodynamics*, 4th ed.; Pearson: 2013.

(6) Kittel, C., *Introduction to Solid State Physics*, 8th ed.; Wiley: 2005.

(7) Hecht, E., *Optics*, 5th ed.; Pearson: 2017.

(8) Mukamel, S., *Principles of Nonlinear Optical Spectroscopy*; Oxford University Press: 1995.

(9) Kaplan, C. J.; Kraus, P. M.; Ross, A. D.; Zürch, M.; Cushing, S. K.; Jager, M. F.; Chang, H.-T.; Gullikson, E. M.; Neumark, D. M.; Leone, S. R. Femtosecond Tracking of Carrier Relaxation in Germanium with Extreme Ultraviolet Transient Reflectivity. *Physical Review B* **2018**, *97*, 1716–1720, DOI: 10.1103/PhysRevB.97.205202.

(10) De Groot, F. High-Resolution X-ray Emission and X-ray Absorption Spectroscopy. *Chemical Reviews* **2001**, *101*, 1779–1808, DOI: 10.1021/cr9900681.

(11) Geneaux, R.; Marroux, H. J. B.; Guggenmos, A.; Neumark, D. M.; Leone, S. R. Transient Absorption Spectroscopy Using High Harmonic Generation: A Review of Ultrafast X-ray Dynamics in Molecules and Solids. *Philosophical Transactions of the Royal Society A: Mathematical, Physical and Engineering Sciences* **2019**, *377*, 20170463, DOI: 10.1098/rsta.2017.0463.

(12) Young, L. et al. Roadmap of Ultrafast X-ray Atomic and Molecular Physics. *Journal of Physics B: Atomic, Molecular and Optical Physics* **2018**, *51*, 032003, DOI: 10.1088/1361-6455/aa9735.

Chapter 2

ELEMENT-SPECIFIC CARRIER AND STRUCTURAL DYNAMICS USING TRANSIENT EXTREME ULTRAVIOLET AND SOFT X-RAY SPECTROSCOPY

Core-level spectroscopy provides energy-resolved information on the local electronic structure environment of the probed element. Challenging direct interpretation of underlying chemical and physical dynamics, the extensive information contained in the core-level spectra is distorted by the perturbation of the core-valence exciton created by the measuring electronic transition. The spectral regime of lower energy core-level excitations, including the extreme ultraviolet (XUV) and soft X-ray (SXR) regimes, are sensitive to coupled carrier-structural dynamics occurring in the material. By employing linear absorption or reflection techniques together with theoretical methods calculating the core-valence excitonic interaction, core-level probes excels at separating carrier and structural in molecular systems and materials. This chapter discusses the unique advantages of XUV and SXR spectroscopies for extracting carrier and structural dynamics in solar energy materials.

This chapter is adapted with permission from:

Liu, H.; Klein, I. M.; Michelsen, J. M.; Cushing, S. K. Element-Specific Electronic and Structural Dynamics Using Transient XUV and Soft X-ray Spectroscopy. *Chem* **2021**, *7*, 2569–2584, DOI: `10.1016/j.chempr.2021.09.005`.

2.1 Abstract

Transient extreme ultraviolet and soft X-ray absorption techniques can measure element-specific ultrafast carrier and structural dynamics in materials or multilayer junctions. However, interpretation of the excited state spectra is not straightforward. The core-hole couples with valence states, distorting the measured spectra. In this perspective, we describe the implementation and interpretation of experiments. This description includes a guide of how to design a transient XUV / soft X-ray spectroscopy experiment by choosing a suitable edge and corresponding X-ray sources. We particularly focus on the rising use of XUV spectroscopy for understanding solar energy materials, such as measurements of polaron formation, electron and hole kinetics, and layer-resolved charge transport in junctions. The ability to measure photoexcited carriers in each layer of a multilayer junction, as well as associated reaction products, could prove particularly impactful in the study of molecules, materials, and their combinations that lead to functional devices in photochemistry and photoelectrochemistry.

2.2 Introduction

To understand photochemical and photoelectrochemical processes, a complete measurement of excitation, thermalization, transport, and recombination of charge carriers is needed.[1, 2] Dynamics on the femtosecond to nanosecond timescale can be deterministic in defining a device's overall performance.[3–10] Capturing the full variety of coupled electronic and structural dynamics is a challenging task for a single experimental tool. This hurdle is especially true when materials and molecules are combined in the active junctions of solar energy devices.[11–14] Transient XUV absorption spectroscopy can separate electron and hole dynamics from the vibrational modes that lead to their relaxation and scattering.[15, 16] When a sample includes multiple elemental edges, the photoexcited dynamics can be separated by atomic contribution.[15–17] In a multi-element junction, the photoexcited dynamics can be separated into each layer and the transport of charge carriers and thermal energy can then be mapped throughout a full device.[12–14] Charge-selective contacts, plasmonic or hot carrier junctions, light absorber/catalyst interfaces, and their reaction products can be studied in their entirety.

Transient XUV and X-ray spectroscopy also brings unique challenges for interpreting experimental data.[18] The X-ray pulse excites a core-level transition to a valence state leaving behind a core-hole. The core-hole couples with valence states, perturbing the measured X-ray spectrum from the underlying orbitals or density of

states.[18] The formation of core-valence excitons can therefore obscure electron and hole occupations. On the other hand, the core-valence exciton can allow structural information to be inferred through changes in bonding lengths and valence states.[4, 19] The energetically narrower valence states in molecules lead to easier to interpret transient X-ray absorption spectra.[19] In a crystal, however, the complexity of the valence and conduction bands with screening and many-body effects obfuscates the measurement, placing a higher demand on theory for proper interpretation.[20, 21] While multiple theoretical approaches exist for predicting the ground state X-ray structure accurately,[18, 20–22] the prediction of excited state dynamics over femtosecond to nanosecond timescales is still an ongoing development.[23]

In this perspective, we emphasize the capabilities and challenges of transient XUV absorption and reflection spectroscopy. We hope to motivate new researchers in relevant fields to consider the technique when studying complex photoexcited dynamics, while also giving an up-to-date picture on how to interpret measured photoexcited changes. In particular, we highlight transient XUV spectroscopy because its measurement of delocalized valence dynamics has led to growing popularity for measuring solar energy materials.[4, 12–14, 24–26] The capability of transient XUV spectroscopy to simultaneously measure photoexcited electron and hole dynamics makes it an extremely valuable tool for the development of solar energy materials.[17, 25–28] Additionally, the table-top setup allows for flexible instrument development and could be valuable in the broader materials science community. We discuss several representative cases—polarons,[4, 10] hot carriers,[24–26, 29] and nanoscale junctions[12–14]—where ultrafast electronic and structural dynamics determine macroscopic device function on longer timescales. Although the examples chosen represent transient XUV spectroscopy, similar concepts can be applied to soft or hard X-rays spectroscopy with absorption edges at higher energies. For more detailed reviews on ultrafast hard X-ray absorption spectroscopy and recent spectroscopy advances of free-electron lasers, we encourage readers to check the following references.[30, 31] Our goal is to help the reader decide which transient X-ray absorption experiments could be most helpful, while also providing fundamental insight into why photoexcited XUV absorption edges appear the way they do.

2.3 Background

Photoexcitation raises the energy of an electron, putting it into a non-equilibrium state. The non-equilibrium charge density leads to many-body electronic interac-

tions and couples with vibrational states. The resulting coupled electronic and structural dynamics are the heart of photochemical processes.[1, 2] Ultrafast charge carrier dynamics do not necessarily affect the overall efficiency of a solar energy device. Often, carriers thermalize and couple to vibronic states on sufficiently short timescales that their effects on the overall device performance can be ignored. Other times, as is the case for polaron formation or inter-system crossings, the coupled electronic-structural dynamics on ultrafast timescales determine overall device functionality.[3–5, 10, 32] Most next-generation solar energy devices attempt to extract more energy per incident photon by relying on ultrafast non-equilibrium dynamics instead of ignoring them.[3, 6, 7] For example, non-equilibrium vibronic states can tune the selectivity of certain reactions and products in molecular catalysts.[33, 34] The excess kinetic energy of photoexcited hot electrons and holes can boost device efficiency.[6, 7] The light-induced hybridization or creation of new states could potentially drive hydrogen evolution or CO_2 reduction. Measuring these ultrafast dynamics is therefore an important step for the implementation of next-generation solar energy devices.

Ultrafast spectroscopy describes a class of pulsed laser-based techniques that are used to measure photoinduced ultrafast dynamics.[35] Generally, one or multiple laser pulses photoexcite a sample, followed by another laser pulse that probes the changes in the absorption or reflection of the sample. The probe pulse measures the electronic and vibrational changes from the photoexcitation. Varying the time delay between the pump and probe pulses enables the real-time observation of photoexcited dynamics. The ideal measurement approach would be to pick a probe wavelength that matches the transition state or resonant feature of interest. However, when using ultraviolet, visible, or infrared light as a probe, overlapping spectral features in the valence states can make it difficult to deconvolute the electronic and vibrational dynamics, especially in the multi-element compounds or integrated multi-layer samples common in photoelectrochemistry.[11] Electron and hole dynamics are also difficult to separate in the signal because their joint density of states is measured. Further, it is helpful to isolate the photoexcited dynamics in terms of different dopants or atomic species. Transient X-ray spectroscopy aims to overcome these issues by probing a core-to-valence transition instead of the valence-valence transition or a vibrational resonance of traditional optical spectroscopy (Figure 2.1).

Core-level transitions span energies from tens of eV to tens of keV. Elements have multiple edges (or core-to-valence transitions) within this broad energy range. The
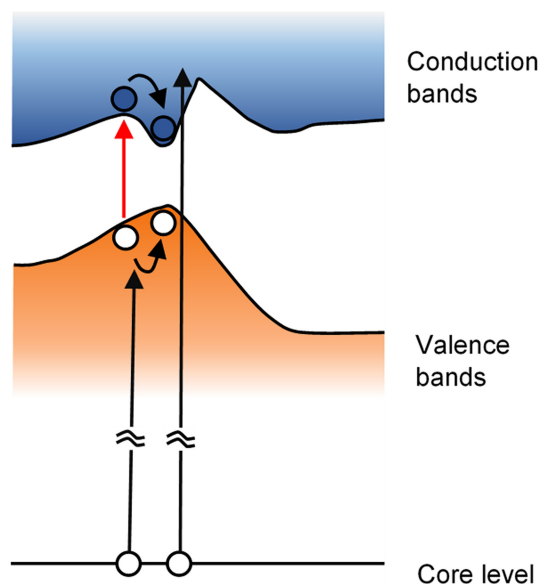
Figure 2.1: Simplified depiction of a time-resolved X-ray absorption experiment. The red arrow indicates transitions with optical pulses, while the broken black arrows indicate an X-ray transition from a core level. The optical pulse excites valence electrons and then the XUV pulse probes the ensuing photodynamics. X-ray pulses can independently probe the electron and hole dynamics.

most important step in designing a transient XUV / X-ray experiment is to select an appropriate absorption edge in the material. Selection of an edge depends on dipole allowed transitions and the dynamics of interest. In solids, the orbital contributions to the valence density of states must be considered for the dipole selection rules. Probing different dipole-allowed transitions of the same element can provide different information about the photoexcited dynamics. For example, low energy XUV photons <100 nm (10-100 nm) probe the delocalized valence dynamics but can only infer structural information through changes in core-valence excitons and multiplet effects.[4, 13, 25, 26, 29] While harder to interpret because of the strong core-valence coupling and multiplet effects, the resulting features allow electrons and holes to be measured simultaneously with strong structural distortions such as polarons.[4, 10, 17, 25–27, 36] On the other hand, high energy hard X-rays at several keV (sub-nm) give atomic-site specific electronic dynamics as well as direct structural information.[18, 31, 37] Soft X-rays fall between XUV and hard X-rays in terms of the probed valence dynamics, again only able to infer structural dynamics by changes in valence couplings[19].

The edge energy also largely determines what XUV/X-ray source is best suited for

the experiment. There are various experimental methods for generating ultrashort X-ray pulses for transient measurements. An X-ray free-electron laser (XFEL) or a synchrotron facility can generate hard X-rays above 1 keV.[38] XFEL, synchrotron, and table-top XUV experiments start to overlap at intermediate soft X-ray energies from 300 eV to 1 keV.[39] Ultrashort, coherent XUV pulses are generally created from a table-top setup using a scheme known as high-harmonic generation (HHG).[40] Whereas synchrotrons and XFELs modulate relativistic free electrons to create X-rays, HHG uses the strong electric field of an optical pulse to photoionize, accelerate, and recombine electrons from a noble gas atom to create X-rays.[40] Since HHG is a coherent process, the spatial and temporal characteristics of the driving pulse are preserved in the XUV pulses that are generated.[41, 42] The resulting broadband XUV pulse duration can be significantly shorter (attoseconds) than the driving optical pulse (femtoseconds).[41] The broad bandwidth of HHG emission makes it useful for measuring multiple atomic edges in one measurement.

A few comments should be made on the practical challenges of table-top XUV/soft X-ray sources. At XFELs and synchrotron sources, experimental difficulties center around limited access time and the inability to construct extensive experiment-specific apparatuses at the facility. For table-top XUV experiments, unlimited access is traded for low XUV/soft X-ray fluxes. In general, the HHG process has a conversion efficiency of $10^{-5} \sim 10^{-7}$ with commonly used noble gases and <20 fs optical driving pulses. Even with high intensity lasers, the produced XUV flux from HHG is limited to the pJ to nJ range.[43] The low conversion efficiency of the HHG process and its reliance on peak intensity adds to the cost and complexity of the experiment. The low flux and short absorption depth of XUV radiation (~100 nm for p-block and ~10 nm for d-block elements) also necessitate special sample preparation. These samples can include transmission measurements on a silicon nitride or diamond window,[4, 25, 26] reflection measurements on smooth solid samples,[10, 13, 27] or few- and sub-micron liquid jet methods.[44–47] Signal to noise ratios allow resolution of transient changes on the order of a few mOD with multiple hours of data acquisition using an XUV CCD spectrometer. Better signal to noise ratios are possible through lock-in detection with an XUV photodiode,[48] but the better signal to noise ratio must be balanced against now having to take thousands of scans at different energies to replace a CCD image.

2.4 Application in solar energy materials

Photocatalytic reactions limited by local charge-trapping (small polaron formation)

Small polaron formation occurs when an electron or hole interacts with a polar lattice to localize the respective wavefunction at a single atomic site.[4, 5, 10] The localization occurs through a distortion in the surrounding bonds. The transformation from a free electron-like wave to a trapped, defect-like charge severely limits charge carrier mobility and increases recombination events. There is a growing belief, backed by transient XUV measurements, that photoexcited small polaron formation explains why metal oxide photocatalysts have never reached the photoconversion efficiencies suggested by their band gap.[4, 10] Small polarons are especially prevalent in transition metals with partially-filled d-orbitals because of the orbitals' localized nature (Fe containing compounds, for example). The localized d-orbitals lead to efficient molecular catalysis but also have a small energy cost for the formation of a small polaron. For largely unfilled or nearly fully filled d-orbitals (e.g. TiO_2 and ZnO), large polarons are formed.[49] Large polarons refer to the fact that the trapped charge and the associated lattice distortion is extended over multiple unit cells to the point where it is only a slight impediment to charge transport.[49–52] Photoexcited polaron formation is still an active area of research, and many intermediate cases such as $BiVO_4$ remain debated.[53] It is becoming increasingly apparent that the photocatalysis community must avoid or reduce small polaron effects to create efficient photocatalysts.

As an XUV application example, recent transient XUV absorption measurements of the Fe $M_{2,3}$ edge of hematite confirm the formation of small polarons around Fe sites in a few picoseconds after optical excitation.[4] Figure 2.2A illustrates the small polaron formation in photoexcited α-Fe_2O_3. Optical excitation induces electron transfer from a negatively charged oxygen site (dark orange) to the positively charged Fe center (light orange). The charge transfer process reduces the Coulomb interaction between the Fe center and the surrounding O atoms. The reduced Coulomb interaction causes a local lattice expansion trapping the electron at the Fe center. The XUV core-level transition is sensitive to its surrounding environment through the core-hole perturbation of the transition state. As will be discussed later, the Fe $M_{2,3}$ edge is dominated by angular momentum coupling of the core-hole to the valence states. The coupling results in multiple peaks that are re-arranged from the unoccupied valence orbitals (Figure 2.2B). The optical charge transfer excitation better screens the core-hole perturbations (which can also be referred to as a change

in oxidation state), so the energy separation between said peaks reduces, producing the blue spectrum in Figure 2.2B immediately after photoexcitation.
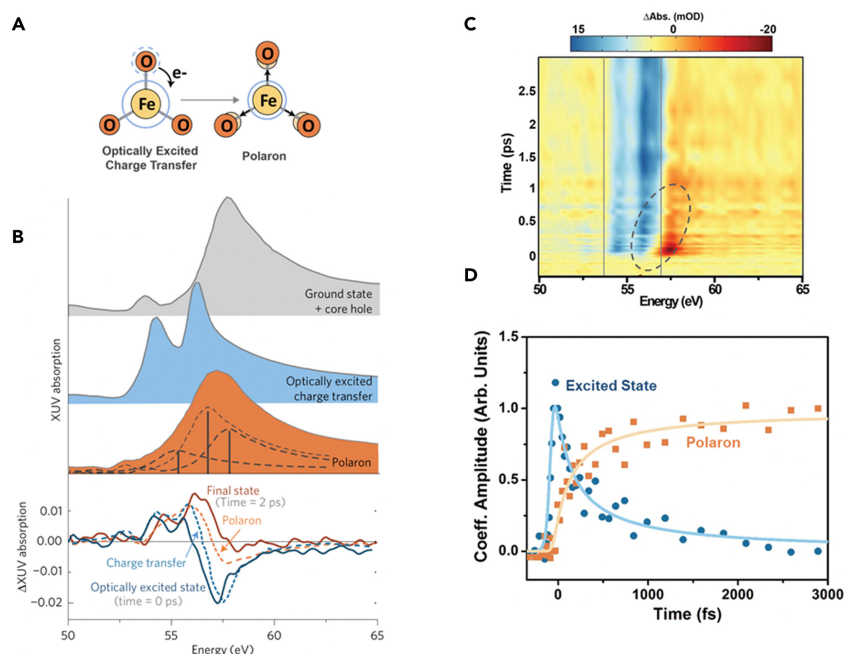
Figure 2.2: (A) Initial excitation of Fe_2O_3 leads to a charge-transfer transition from oxygen (dark orange) to iron (light orange). The initial excited carriers undergo optical-phonon scattering, during which the charge can be trapped by forming a small polaron expanding the lattice locally. (B) XUV absorption spectra of the polaron formation process. The top panel is experimental data; the middle two panels are simulations. Dashed lines represent the contributions of the multiplet splitting and core-hole absorption to the predicted small polaron spectrum. The final panel shows the predicted contributions of charge transfer and the polaron to the differential absorption spectrum (dashed lines) compared to the time = 0 ps and time = 2 ps differential absorption measurements following a 480 nm excitation pulse (solid lines). (C) The resulting transient XUV absorption measurement. Following photoexcitation, the differential absorption reveals regions of increased and decreased absorption around 55 and 56 eV. The energy of the zero crossing between the areas of increased (blue) and decreased (red) absorption shifts on a ~500 fs timescale and is circled for clarity. (D) The experimental time = 0 ps and time = 2 ps slices are used to extract the amplitude of the charge-transfer and small polaron state using a multivariate regression of the experimental data. These amplitudes are fitted with a rate equation model for small polaron formation (solid lines). Reprinted with permission from Carneiro et al.[4] Copyright 2017 Macmillan Publishers Limited, part of Springer Nature.

The polaron formation creates a local anisotropic lattice distortion that breaks the degeneracy of Fe 3p core level. The sub-picosecond shift in the differential ab-

sorption (Fig. 2.2B, bottom panel) corresponds to the resulting change to the XUV absorption (Fig. 2.2C). Hence, the polaron formation rate relative to the charge transfer state is apparent in the differential absorption, as shown in Fig. 2.2C and D.

After decomposition of the differential absorption, the small polaron formation is measured to occur in under 100 fs (Figure 2.2D), matching the first electron-phonon scattering events. Importantly, the small polaron state persists until the photoexcited electron and hole recombine. The few picosecond polaron formation will therefore determine any later photocatalytic steps. Interestingly, polaron formation has been measured not to be influenced by grain boundaries or defect states. Small polaron formation is an intrinsic property of the lattice that cannot be removed by better quality materials alone. Bulk and surface polaron formation occur on slightly different timescales, with bulk polaron formation occurring with a time constant of 90 fs and surface polarons forming with a time constant of 250 fs.[4, 36] Molecular functionalization of the hematite surface has also been shown to change the lattice reorganization and polaron stabilization energies, but polarons still form with rates between 146 fs for OMe-PPA-Fe_2O_3 and 250 fs for hydroxyl-Fe_2O_3.[36] Furthermore, comparing small polaron formation in hematite and goethite (α-FeOOH) has shown that small changes in ligands and crystal structure have a significant effect on formation rates, with polarons forming in 180 ± 30 fs in goethite nanorods and 90 ± 5 fs in a hematite thin film.[54] Engineering materials to remove polaronic effects remains as an outstanding question for photocatalysis and photoelectrochemistry.

Energy-resolved electron and hole kinetics

As highlighted by small polaron formation, controlling the relaxation pathways of photoexcited carriers is crucial for optimizing solar energy devices. Efficient extraction of the excess kinetic energy of hot (non-thermalized) electrons and holes can overcome the theoretical Shockley-Queisser efficiency limit.[3, 6, 7] Hot electrons and holes created by plasmonic nanoparticles can create new photoproducts not reachable with thermalized carriers.[8] The ability of transient X-ray absorption spectroscopy to separately measure the electron and hole energies as a function of time is very useful for these applications, whether the device utilizes thermalized or non-thermalized carriers. To be clear, X-ray spectroscopy measures the momentum summed electron and hole energies, not to be confused with angle resolved photoemission spectroscopy (ARPES). However, X-rays offer different benefits than ARPES in terms of penetration depth,[12] measuring electronic and structural dynamics simultaneously,[4, 29] element specificity,[17] and the ability to measure
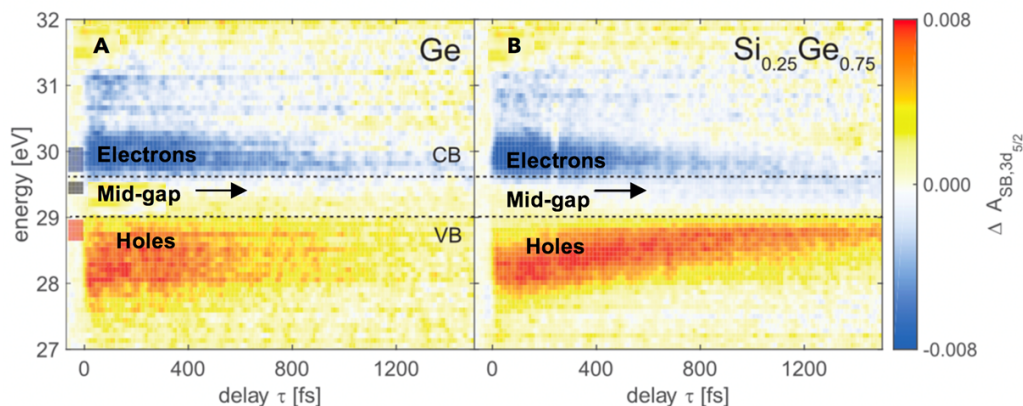
insulating or oxidized samples.[55]

Figure 2.3: Time-resolved measurement of electron and hole dynamics in a germanium nanocrystal thin film (A) and silicon-germanium alloy (B). (A) Carrier dynamics in nanocrystalline germanium reveal the relaxations and decays of photoexcited carriers in the valence band (VB) and conduction band (CB). The hole, mid-gap, and electron states are labelled on the plot. (B) The electron and hole dynamics are different in a Si:Ge alloy, and an additional weak feature is measured for photoexcited electron filling of the mid-gap states (indicated by the black arrow. Reprinted from Zürch et al.[26] Licensed under a Creative Commons Attribution (CC BY) license.

Figure 2.3 shows the measured transient XUV absorption at the germanium $M_{4,5}$ edge of a germanium thin film (A)[25] and a $Si_{0.25}Ge_{0.75}$ alloy (B).[26] In this experiment, a visible-to-near-IR femtosecond pulse photoexcites the thin film samples. The photoexcitation creates free electrons and holes in the conduction bands and valence bands, respectively. The holes in the valence bands result in new XUV transitions and appear in the measurement as a positive (red) contribution. Similarly, photoexcited electrons in the conduction band will block existing XUV transitions, reducing the XUV absorption in the measured spectrum (blue). Electron and hole dynamics are therefore separated by the band gap, as modified by core-valence excitons, in the transient XUV spectra (Figure 2.3A and B). In this figure, a constant energy shift has been removed from the differential absorption to give a better picture of the electron and hole dynamics. A shift of the entire edge to lower energy is measured because the photoexcited state changes the screening of the core-hole perturbation (similar to band gap renormalization in optical excitation).

From the processed differential absorption, electrons are measured to thermalize quicker than holes over a one picosecond timescale. The slower hole thermalization

is expected because of the higher effective mass of holes. The holes also have a higher initial energy because of where the optical excitation occurred within the band structure of Ge and the SiGe alloy. The kinetics of the SiGe alloy (Figure 2.3B) can be compared to measurements of Ge alone (Figure 2.3A). After the carriers are thermalized, a filling of the mid-gap defect states in the alloy is measured (Figure 2.3B). The decreasing amplitude in the differential absorption also measures the electron and hole recombination.

Concerning defect and dopant state measurements, the current signal to noise ratio limits experiments to the 1 mOD level for carrier excitation densities in the 10^{19-20} carriers/cm^3 range (corresponding to a one-thousandth excitation of an average atomic density of 10^{22-23}atoms/cm^3). Assuming a comparatively high contrast XUV absorption between the dopant or defect state and the host material, such as a transition metal M edge in a p-orbital host, this estimation suggests that a few percent doping level can be measured. The estimate is in line with the ability to measure defect state occupation in an alloy like SiGe with a high defect density.[26] Measuring how a few percent dopant or defect states affect the photoexcited dynamics of an alloy is a promising direction for the transient X-ray techniques.

Carrier kinetics have been measured in a range of materials using transient XUV spectroscopy.[24, 56] Figure 2.4A shows the differential absorption of Si from which electron and phonon dynamics are measured. Comparing Figure 2.4 to Figure 2.3 highlights the trade-off between different core-level transitions. Interpretation of the Si $L_{2,3}$ edge is dominated by core-valence excitons, requiring a more in-depth theoretical treatment. However, the core-valence excitons provide sensitivity to structural changes such as acoustic phonons,[29] whereas they are more difficult to interpret in the Ge $M_{4,5}$ edge at lower energy. Comparison of the electron and acoustic phonon dynamics then allows inference of the optical phonon dynamics. A Bethe-Salpeter equation (BSE) approach[21] was developed to predict the change in the photoexcited transient XUV spectra of Si. The electron population versus time, the thermalization of the electrons, and the acoustic phonon generation can then be extracted from the differential absorption spectrum (Figure 2.4B).[29] The extracted kinetics match those of known silicon scattering rates from optical measurements, but in transient XUV spectroscopy the electron and phonon dynamics can be measured at the same time. Valley-dependent scattering rates can also be obtained by changing the excitation wavelength in the measurement.[29] The measurements of the Si $L_{2,3}$ edge are good examples of where intuitive interpretation
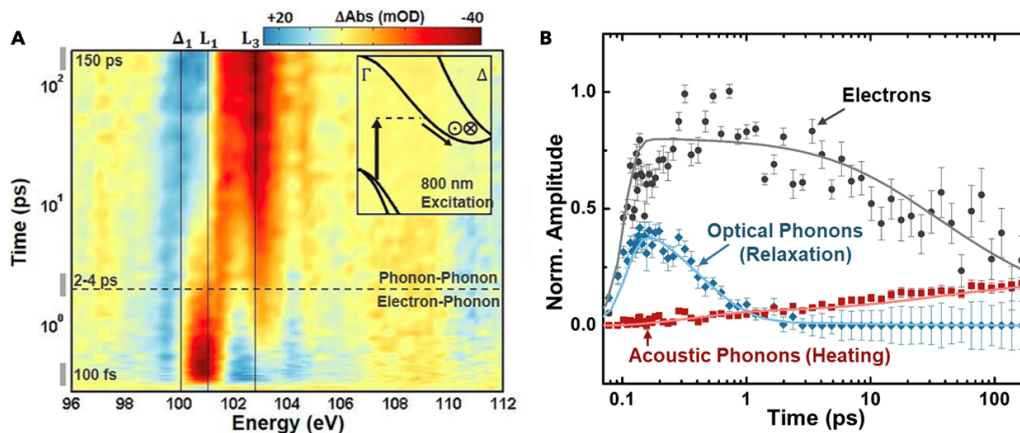
Figure 2.4: Time-resolved XUV spectroscopy of the silicon $L_{2,3}$ edge. (A) The differential absorption is shown on a logarithmic time scale from 0 to 200 ps for 800 nm excitation. The inset represents some of the possible excitation and scattering pathways for the photoexcited electrons. The in and out of plane arrows indicate where inter-valley scattering between degenerate valleys is possible. The cross-over time between electron-phonon scattering and phonon-phonon scattering is also indicated by the dashed horizontal line. (B) Time-dependent carrier density, lattice deformation, and thermal lattice expansion are extracted from a non-linear fit of the measured excited state XUV absorption in A, following modeling of the XUV spectrum with the Bethe-Salpeter equation (BSE). The solid lines show the predictions of a three-temperature model for the carrier density, optical phonons, and acoustic phonons. The data points refer to the quantities extracted from the experimental data, with error bars representing the standard error of the fit to the experimental data. The non-linear fit is weighted by the experimental uncertainty. The scatter of the points is representative of the experimental noise. The thermal lattice expansion from acoustic phonons is approximated as an isotropic lattice expansion in the BSE model. The log scale of time is offset by 100 fs for visualization. Reprinted from Cushing et al.[29] Licensed under a Creative Commons Attribution (CC BY) license.

based on increased and decreased absorption fail without more in-depth theoretical modeling of core-valence coupling. The more complex ab initio methods, however, do allow for larger classes of materials to be interpreted than material-specific toy models. Also, once a material is theoretically modeled, future experiments can then be analyzed with simpler decomposition or lineout methods.

Charge transfer in multilayer devices

Solar energy devices rely on multi-materials junctions to separate and transport electrons and holes.[57] The critical interfaces within a device are the charge-selective

contacts in a photovoltaic cell or the semiconductor-catalyst-electrolyte interface of a photoelectrochemical cell.[11, 57] Multiple charge transport events, recombination, thermalization, and oxidation-reduction reactions occur from femtosecond to second timescales.[1, 8, 11, 57] Measuring the ultrafast photo-dynamics of buried interfaces is a challenging but valuable spectroscopic task for these devices. While charge transfer is readily measured in two-component systems[17, 58] (such as between solids and quantum dots or molecules), adding the metal contacts and multiple broadband absorbers of a full solar energy device makes transient optical measurement non-trivial. Element-specific transient XUV measurements, on the other hand, can track the photoexcitation and electronic-structural coupling that leads to both charge and heat transport between multiple layers.[24, 29] The XUV penetration depth can also be varied as a function of incident angle to differentiate surface and bulk dynamics or same-element junctions, such as p-n and p-i-n doped materials. Comparison of the measured kinetics of different elemental edges (or as a function of incidence angle) leads to the direct calculation of transport properties as long as the layer thicknesses are known. The ultrafast transient XUV measurements are therefore directly comparable to the results of device averaged bulk electrical measurements.[12]

As an example, Figure 2.5A shows the carrier transport processes in a p-Si/TiO$_2$/Ni photoelectrode geometry.[12] An 800 nm near-infrared pulse photoexcites the Si. The built-in-field of the junction then leads to transfer of the photogenerated holes of Si to the Ni layer (Figure 2.5B). The hole transport process is measured by a negative energy shift in the Ni M$_{2,3}$ edge because the added electron screens the many-body core-valence interaction in the metal (which corresponds to the quasi-Fermi level energy). The Ni shift compared to the Si dynamics measures ballistic transport without occupation in the TiO$_2$ in the first ~100 fs (Figure 2.5B). Picoseconds later, holes in the Ni diffuse back through the TiO$_2$ to the Si. This back-diffusion of holes decreases the screening of the core-valence exciton (or increases the Ti oxidation state) which leads to a positive energy shift in the Ti M$_{2,3}$ edge energy. Eventually the holes recombine with electrons, the loss of which is measurable by analysis of the Si edge with the BSE approach as described in the previous section. The summary of the full carrier transport kinetics in this multi-junction layer device is therefore measured as summarized in Figure 2.5B. The holes arrive on the Ni edge after a 33 ± 8 fs delay from the photoexcitation pulse. More quantitatively, the transport properties can be calculated from the kinetics and the ~20 nm thickness of the TiO$_2$ layer. The holes have a tunneling velocity of $(5.8 \pm 1.4) \times 10^7$ cm $\cdot$ s^{-1},
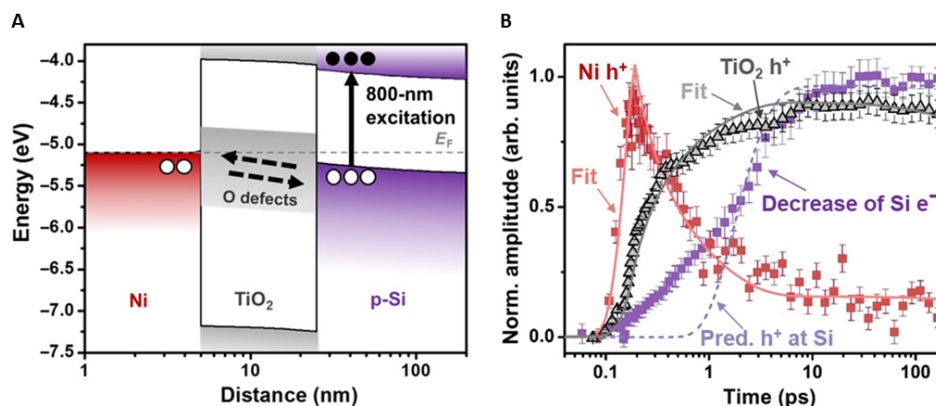
Figure 2.5: (A) The energy level alignment for the metal, oxide, and semiconductor is shown, along with the expected photoexcited hole transfer in the p-type metal-oxide-semiconductor junction. (B) The edge shift kinetics, which indicate the hole kinetics, measured for the TiO_2 (gray triangles) and the Ni (red squares) in the junction are compared to the increase in electron recombination (i.e. decrease in electron signature at the Si edge) in the junction (purple squares). The solid line is a fit to the diffusion equation with a diffusion constant of 1.2 ± 0.1 cm$^2 \cdot$s^{-1} and a surface recombination velocity of 20 ± 50 cm $\cdot$ s^{-1}. The measured decrease in electron density qualitatively tracks the diffusion of holes through the TiO_2. The dashed line represents the predicted (Pred.) arrival of holes at the Si-TiO_2 interface based on the fit diffusion kinetics. Reprinted with permission from Cushing et al.[12]

similar to the velocity of the electrons in the Si, indicating ballistic tunneling. From the calculated built-in field of the junction, the hole mobility is calculated to be 390 ± 100 cm$^2 \cdot$V$^{-1} \cdot$s^{-1}, which is comparable to the established value for 10^{15} cm^2 p-doped Si (450~500 cm$^2 \cdot$V$^{-1} \cdot$s^{-1}).[59] A charge transfer efficiency of 42% is also extracted from the measurement, and a surface recombination velocity at the Si-TiO_2 interface is calculated to be >200 cm/s.

Interfacial hole transfer dynamics have also been reported in other solar junctions, including Fe_2O_3/NiO and Zn/n-GaP junctions.[13, 60] The transient XUV measurement of a Fe_2O_3/NiO heterojunction (Figure 2.6) indicates a hole transfer from the Fe_2O_3 to NiO ~10 ps after photoexcitation.[13] The simultaneous measurement of the Fe $M_{2,3}$ edge and the Ni $M_{2,3}$ edge (Figure 2.6C) indicates the two-step nature of the mechanism. An initial localized excitation on the Fe persists for 680 fs after photoexcitation, after which the hole is injected into NiO after ~10 ps. Transient XUV spectroscopy again gives a detailed microscopic picture of charge transport in
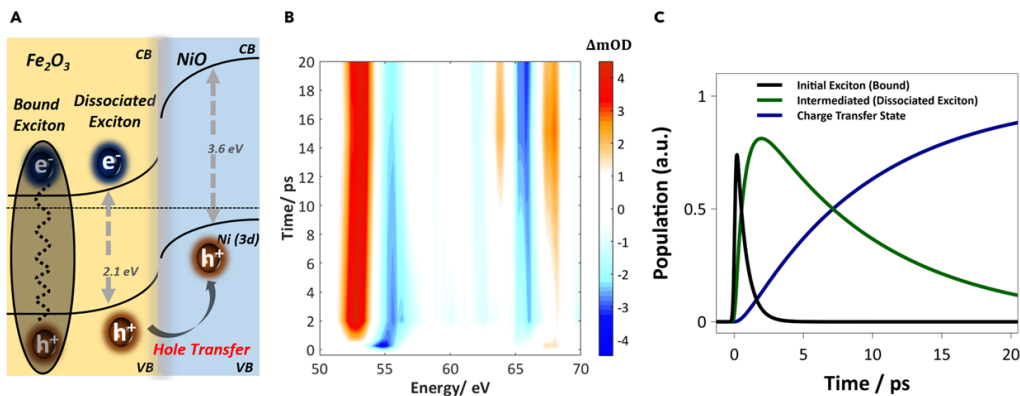
Figure 2.6: (A) Schematic depiction of a two-step sequential mechanism of hole transfer. The interfacial field drives the exciton dissociation in the space charge region of Fe_2O_3/NiO heterojunction. The subsequent hole transfer occurs via the drift of the carrier across the interface. (B) Contour plot showing the experimental transient reflection data of the Fe_2O_3/NiO heterojunction after excitation with 400 nm light. (C) The population of the bound exciton, dissociated exciton, and hole transfer states is obtained from the global fit of data in B. Photoexcitation at 400 nm initially leads to a charge transfer excitation in the Fe_2O_3, which dissociates with a rate constant of k_1 (680 ± 60 fs). The subsequent interfacial hole transfer across to the NiO occurs with a rate constant of k_2 (9.2 ± 2.9 ps). Adapted with permission from Biswas et al.[13]

a multi-layer junction.

Interpreting photoexcited X-ray absorption spectra

The interpretation of photoexcited X-ray absorption spectra requires theoretical modelling to accurately extract charge carrier and structural dynamics, regardless of the energy range used.[18, 20–22] An X-ray probe photon excites a core electron to a valence state, leaving a positively charged localized hole in the core state. As a first approximation, the transition probability of the X-ray, and thus the measured absorption spectrum, would be proportional to the unoccupied valence density of states including dipole selection rules, because of the narrow energy width of the core level. However, the core-hole that is created during the X-ray transition perturbs the final transition valence density of states.[18, 21, 22] The strength and extent of this perturbation determines what information can be extracted from the transient X-ray absorption experiment. The ability to model and predict the core-valence perturbation defines what photoexcited information can be extracted from a transient X-ray absorption measurement.

The general ranking of different core-hole perturbation effects, from strongest to weakest, is angular momentum effects (atomic multiplet and spin orbit effects resulting from the interaction between unpaired valence electrons and the unpaired core electron), ligand field effects on these angular momentum perturbations, and the creation of core-valence excitons between the X-ray excited electron and the core-hole. The ability of the valence orbitals to screen the core-hole perturbations determines the peak amplitudes and spectral shifts within this general ordering, often resulting in XUV absorption spectra that do not follow the form of the valence density of states.[4, 12]
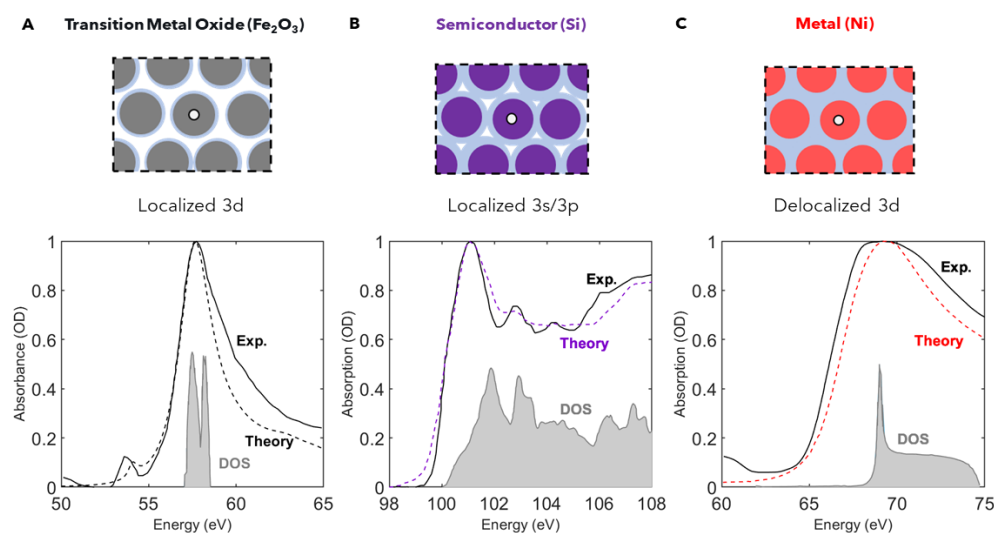
Figure 2.7: (A) In a metal oxide, the localized d levels interact strongly with the core-hole of the XUV transition. The final transition density of states is dominated by atomic multiplet splitting and is therefore distorted from the unoccupied valence states. (B) In a covalent semiconductor, the delocalized electrons shield the core-valence exciton, and the measured experimental absorption is close to the unoccupied density of states. (C) In metals, many-body effects lead to an increased absorption near the Fermi level and a power law tail as compared to the underlying density of states. Adapted with permission from Cushing et al.[12]

For X-ray transitions to localized d-orbitals, such as the M-edge of the first-row transition metals, angular momentum and spin-orbit effects are dominant in the X-ray spectra. Atomic multiplet coupling between the core level and valence states leads to a redistribution of the ground state, unoccupied density of states across tens of eV (Figure 2.7A). Multiplet effects are edge dependent, with multiplet interaction generally being stronger for M edges compared to L edges, while not present in K edges. The angular momentum effects make extracting exact electron and hole

energies more difficult but also make the edge more sensitive to dynamic bonding and structural changes as described earlier for polarons[4]. Screening and ligand field effects determine the exact strength and separation of the peaks. A lower energy peak is therefore not necessarily a lower energy valence orbital. Theoretical methods[20–22] are used to map out to which states the X-ray peaks correspond. A photoexcited change in oxidation state / screening is usually obvious in the measured spectra, such as the ligand to metal charge transfer[4] in Figure 2.2, but the electrons and holes are not spectrally resolved as in Ge (Figure 2.3A).

For elements with s- and p-orbital valence electrons, the angular momentum coupling is moderate. The primary perturbation affecting the X-ray absorption structure is the creation of core-valence excitons. The core-valence exciton is usually narrow in linewidth and shifted lower in energy from the expected orbital with a modulated amplitude. In a molecule, the core-valence exciton is quite pronounced because valence orbitals are highly localized and therefore do not screen the core-hole.[19] In a solid, the delocalized electron and hole wavefunctions can screen the core-hole and weaken the excitons amplitude and energy shift. The XUV spectrum is then more closely (but not exactly) related to the ground state, valence density of states of the material (Figure 2.7B).[24] After photoexcitation, electrons block existing XUV transitions while holes allow new XUV transitions, generically leading to negative and positive peaks in a transient X-ray spectrum.[25, 26] Changes in the occupation and energy of electrons and holes can therefore be measured and extracted, sometimes even without the need for in-depth theoretical modeling as is the case for Ge in Figure 2.3.[25, 26] However, more generally, the change in photoexcited valence occupation screens any core-valence excitons, with the resulting renormalization causing spectral changes across the full XUV absorption, as seen in the Si $L_{2,3}$ edge in Figure 2.7C.[24, 29] In this case, relying only on positive and negative changes in the transient absorption measurement is misleading and in-depth theoretical modeling is needed.

However, intuition about screening of the core-hole does not always hold true. An important case is the X-ray absorption spectrum of metals.[61] For a metal, many-body interactions between the core-hole and free electrons dominate the X-ray absorption. For example, the renormalization from the core-hole creates an exponentially increasing density of states near the Fermi level in the otherwise narrow bandwidth and partially filled d-valence bands. The resultant many-body effect leads to a strong increase in absorption, or "white line effect", at the X-ray edge

energy and a power law decaying tail.[62] The X-ray absorption spectrum is thus broadened and redistributed from the underlying empty orbitals, even though atomic multiplet effects are minor (Figure 2.7C). The shift in the edge with photoexcitation, however, usually aligns with the change in quasi-Fermi level after excitation, allowing average electron or hole energies to be generically extracted (Figure 2.5).

Regardless of the edge or the material, as the photoexcited carriers relax by coupling with vibrational modes (phonons), a longer timescale (10-100 picoseconds) "heating" signal is measured in the transient X-ray spectra that originates from acoustic phonons.[29] A lattice expansion occurs from the anharmonicity of the excited vibrational modes generically from acoustic phonons created by phonon-phonon scattering of optical phonons or direct electron-phonon scattering at energies near the band edge. The resultant lattice expansion decreases the bond hybridization and the band gap of the material, so the interaction of the core-hole with surrounding atoms is decreased and the overall X-ray spectrum is shifted to lower energy.[29] The "heating" feature can be used to study heat transport between materials in a junction, like carrier kinetics in Figure 2.5 and 2.6, but by comparing its kinetics with the change in carrier energy versus time, the electron-optical phonon and the optical-to-acoustic phonon scattering can be kinetically extracted. Phase changes and other lattice distortions are similarly measurable.

While atomic multiplet theory can predict M edge spectra in metal oxides,[63] Bethe-Salpeter Equation (BSE) and time-dependent density functional theory (TDDFT) calculations are rising as a material and edge independent method to accurately predict X-ray edges including multiplet effects and Coulomb screening.[21] First, TDDFT calculations can be used for directly simulating the time evolution of core-holes and valence excitations on the sub-picosecond timescale.[64] This approach gives the real time evolution of the states, predicting attosecond dynamics, but it is computationally expensive for longer timescales. In the second approach, the BSE equation spectrally solves the experimental X-ray spectra but without inherent time dependency.[21] Generally, a DFT calculation is used to calculate the ground state valence orbitals and their occupation. An optional GW approximation step is used to correct the DFT band structure for electron-electron type interactions. The naming of the GW approximation comes from the term symbols used for the Green's function and screening used when calculating the self-energy of a many-body system of electrons. Next, the core-valence excitons and any angular momentum coupling is calculated using the BSE. Two approaches can be taken to predicting the transient

XUV spectrum. First, the time evolution of the excited state can be included from other software packages (like molecular dynamics and Boltzmann transport equation solutions) into the DFT, GW, and BSE steps. The calculations are based on the approximation that the core-hole excitation (attoseconds) is faster than the measured carrier or phonon dynamics (femtoseconds and longer) and are therefore not suitable for attosecond dynamics. Second, generic changes in carrier and phonon occupation can be included in the BSE without a full excited state ab initio calculation, then the experimental spectrum can be back-fit to extract the carrier occupations and structural dynamics. The flexibility of the second approach is useful for experiments on novel or complex materials where time dependent calculations are not feasible. In either case, the BSE approach allows for different components of the core-valence coupled Hamiltonian to be separated, such as contributions from spin-orbit, multiplet splitting, long-range screening, and higher order processes such as bubble/ladder interactions.

2.5   Outlook

This perspective outlines the potential of transient XUV spectroscopy for measuring photoexcited dynamics in solar energy materials. Although only a few materials have been measured to date, the technique is now reaching a maturity that makes it ready for widespread measurement. An important instrumentation development step is to include in situ and environmental cells to match the cutting edge of synchrotron experiments. The ideal measurement would measure the photoexcited dynamics of carriers, charge transfer between the electrode-electrolyte interface, and the associated chemical reaction intermediates and products that form. For example, recent static in situ measurements were taken of the electrochemical CO_2 reduction reaction on a Cu catalyst with X-ray absorption spectroscopy and X-ray diffraction.[65] In situ measurements are traditionally more difficult with table-top XUV experiments because of the limited penetration depth of the XUV photon with respect to water. However, table-top sources are now pushing into the water window (282~533 eV) with sufficient flux for transient experiments in the liquid phase.[39] This energy coverage also allows the study of organic elements. Transient XUV spectroscopy could also be significant for measuring the alloyed and multiple-element catalysts critical for photoelectrochemical cells. As signal to noise ratios continue to improve, the ability to measure the role of trace defect and dopant states is also on the horizon.

In addition to linear X-ray absorption spectroscopy, novel nonlinear X-ray methods

are emerging as a promising field for both fundamental light-matter interaction and material characterization.[66–70] Recent developments of intense X-ray sources at larger facilities and on the table-top are now making nonlinear X-ray measurements possible. X-ray transient grating spectroscopy[67] can measure element-specific vibrational, magnetic, or electronic transport. XUV second harmonic generation has measured atomic displacement with sub-angstrom spatial resolution.[66] X-ray sum frequency generation is allowing an element-specific addition to studying interfaces.[66, 67] X-ray wave mixing processes are also starting to reach the level of complexity needed for true two-dimensional spectroscopy studies of coupled excitations.[67, 69] Chiral and circularly polarized X-rays are also reaching a maturity for studying spin dependent phenomenon.[71, 72]

References

(1) Scholes, G.; Fleming, G.; Olaya-Castro, A.; Grondelle, R. Lessons from Nature about Solar Light Harvesting. *Nature Chemistry* **2011**, *3*, 763–774.

(2) Wang, Y.; Vogel, A.; Sachs, M.; Sprick, R.; Wilbraham, L.; Moniz, S.; Godin, R.; Zwijnenburg, M.; Durrant, J.; Cooper, A. Current Understanding and Challenges of Solar-Driven Hydrogen Generation Using Polymeric Photocatalysts. *Nature Energy* **2019**, *4*, 746–760.

(3) Smith, M.; Michl, J. Singlet Fission. *Chemical Reviews* **2010**, *110*, 6891–6936.

(4) Carneiro, L. M.; Cushing, S. K.; Liu, C.; Su, Y.; Yang, P.; Alivisatos, A. P.; Leone, S. R. Excitation-Wavelength-Dependent Small Polaron Trapping of Photoexcited Carriers in α-Fe_2O_3. *Nature Materials* **2017**, *16*, 819–825, DOI: `10.1038/nmat4936`.

(5) Pastor, E.; Park, J.-S.; Steier, L.; Kim, S.; Grätzel, M.; Durrant, J. R.; Walsh, A.; Bakulin, A. A. In Situ Observation of Picosecond Polaron Self-Localisation in α-Fe_2O_3 Photoelectrochemical Cells. *Nature Communications* **2019**, *10*, 3962, DOI: `10.1038/s41467-019-11767-9`.

(6) Garin, M.; Heinonen, J.; Werner, L.; Pasanen, T. P.; Vähänissi, V.; Haarahiltunen, A.; Juntunen, M. A.; Savin, H. Black-Silicon Ultraviolet Photodiodes Achieve External Quantum Efficiency above 130%. *Physical Review Letters* **2020**, *125*, 117702, DOI: `10.1103/PhysRevLett.125.117702`.

(7) Schaller, R.; Agranovich, V.; Klimov, V. High-Efficiency Carrier Multiplication through Direct Photogeneration of Multi-Excitons via Virtual Single-Exciton States. *Nature Physics* **2005**, *1*, 189–194.

(8) Brongersma, M.; Halas, N.; Nordlander, P. Plasmon-Induced Hot Carrier Science and Technology. *Nature Nanotechnology* **2015**, *10*, 25–34.

(9) Cushing, S. K.; Li, J.; Meng, F.; Senty, T. R.; Suri, S.; Zhi, M.; Li, M.; Bristow, A. D.; Wu, N. Photocatalytic Activity Enhanced by Plasmonic Resonant Energy Transfer from Metal to Semiconductor. *Journal of the American Chemical Society* **2012**, *134*, 15033–15041, DOI: `10.1021/ja305603t`.

(10) Bandaranayake, S.; Hruska, E.; Londo, S.; Biswas, S.; Baker, L. R. Small Polarons and Surface Defects in Metal Oxide Photocatalysts Studied Using XUV Reflection–Absorption Spectroscopy. *The Journal of Physical Chemistry C* **2020**, *124*, 22853–22870, DOI: `10.1021/acs.jpcc.0c07047`.

(11) Tran, P. D.; Wong, L. H.; Barber, J.; Loo, J. S. C. Recent Advances in Hybrid Photocatalysts for Solar Fuel Production. *Energy & Environmental Science* **2012**, *5*, 5902–5818, DOI: `10.1039/c2ee02849b`.

(12) Cushing, S. K.; Porter, I. J.; Roulet, B. R. de; Lee, A.; Marsh, B. M.; Szoke, S.; Vaida, M. E.; Leone, S. R. Layer-Resolved Ultrafast Extreme Ultraviolet Measurement of Hole Transport in a Ni-TiO_2-Si Photoanode. *Science Advances* **2020**, *6*, eaay6650, DOI: `10.1126/sciadv.aay6650`.

(13) Biswas, S.; Husek, J.; Londo, S.; Fugate, E. A.; Baker, L. R. Identifying the Acceptor State in NiO Hole Collection Layers: Direct Observation of Exciton Dissociation and Interfacial Hole Transfer across a Fe_2O_3/NiO Heterojunction. *Physical Chemistry Chemical Physics* **2018**, *20*, 24545–24552, DOI: `10.1039/C8CP04502J`.

(14) Marsh, B. M.; Vaida, M. E.; Cushing, S. K.; Lamoureux, B. R.; Leone, S. R. Measuring the Surface Photovoltage of a Schottky Barrier under Intense Light Conditions: Zn/p-Si(100) by Laser Time-Resolved Extreme Ultraviolet Photoelectron Spectroscopy. *The Journal of Physical Chemistry C* **2017**, *121*, 21904–21912, DOI: `10.1021/acs.jpcc.7b06406`.

(15) Kraus, P. M.; Zürch, M.; Cushing, S. K.; Neumark, D. M.; Leone, S. R. The Ultrafast X-ray Spectroscopic Revolution in Chemical Dynamics. *Nature Reviews Chemistry* **2018**, *2*, 82–94, DOI: `10.1038/s41570-018-0008-8`.

(16) Geneaux, R.; Marroux, H. J. B.; Guggenmos, A.; Neumark, D. M.; Leone, S. R. Transient Absorption Spectroscopy Using High Harmonic Generation: A Review of Ultrafast X-ray Dynamics in Molecules and Solids. *Philosophical Transactions of the Royal Society A: Mathematical, Physical and Engineering Sciences* **2019**, *377*, 20170463, DOI: `10.1098/rsta.2017.0463`.

(17) Attar, A. R.; Chang, H.-T.; Britz, A.; Zhang, X.; Lin, M.-F.; Krishnamoorthy, A.; Linker, T.; Fritz, D.; Neumark, D. M.; Kalia, R. K.; Nakano, A.; Ajayan, P.; Vashishta, P.; Bergmann, U.; Leone, S. R. Simultaneous Observation of Carrier-Specific Redistribution and Coherent Lattice Dynamics in 2H-$MoTe_2$ with Femtosecond Core-Level Spectroscopy. *ACS Nano* **2020**, *14*, 15829–15840, DOI: `10.1021/acsnano.0c06988`.

(18) De Groot, F. High-Resolution X-ray Emission and X-ray Absorption Spectroscopy. *Chemical Reviews* **2001**, *101*, 1779–1808, DOI: `10.1021/cr9900681`.

(19) Attar, A.; Bhattacherjee, A.; Pemmaraju, C.; Schnorr, K.; Closser, K.; Prendergast, D.; Leone, S. Femtosecond X-ray Spectroscopy of an Electrocyclic Ring-Opening Reaction. *Science* **2017**, *356*, 54–59.

(20) Ankudinov, A.; Ravel, B.; Rehr, J.; Conradson, S. Real-Space Multiple-Scattering Calculation and Interpretation of X-ray-Absorption Near-Edge Structure. *Physical Review B* **1998**, *58*, 7565–7576.

(21) Vinson, J.; Rehr, J. J.; Kas, J. J.; Shirley, E. L. Bethe-Salpeter Equation Calculations of Core Excitation Spectra. *Physical Review B* **2011**, *83*, 115106, DOI: `10.1103/PhysRevB.83.115106`.

(22) De Groot, F. Multiplet Effects in X-ray Spectroscopy. *Coordination Chemistry Reviews* **2005**, *249*, 31–63.

(23) Zhou, J.-J.; Park, J.; Lu, I.-T.; Maliyov, I.; Tong, X.; Bernardi, M. PER-TURBO: A Software Package for *Ab Initio* Electron–Phonon Interactions, Charge Transport and Ultrafast Dynamics. *Computer Physics Communications* **2021**, *264*, 107970, DOI: `10.1016/j.cpc.2021.107970`.

(24) Cushing, S. K.; Lee, A.; Porter, I. J.; Carneiro, L. M.; Chang, H.-T.; Zürch, M.; Leone, S. R. Differentiating Photoexcited Carrier and Phonon Dynamics in the Δ, *L*, and Γ Valleys of Si(100) with Transient Extreme Ultraviolet Spectroscopy. *The Journal of Physical Chemistry C* **2019**, *123*, 3343–3352, DOI: `10.1021/acs.jpcc.8b10887`.

(25) Zürch, M.; Chang, H.-T.; Borja, L. J.; Kraus, P. M.; Cushing, S. K.; Gandman, A.; Kaplan, C. J.; Oh, M. H.; Prell, J. S.; Prendergast, D.; Pemmaraju, C. D.; Neumark, D. M.; Leone, S. R. Direct and Simultaneous Observation of Ultrafast Electron and Hole Dynamics in Germanium. *Nature Communications* **2017**, *8*, 15734, DOI: `10.1038/ncomms15734`.

(26) Zürch, M.; Chang, H.-T.; Kraus, P. M.; Cushing, S. K.; Borja, L. J.; Gandman, A.; Kaplan, C. J.; Oh, M. H.; Prell, J. S.; Prendergast, D.; Pemmaraju, C. D.; Neumark, D. M.; Leone, S. R. Ultrafast Carrier Thermalization and Trapping in Silicon-Germanium Alloy Probed by Extreme Ultraviolet Transient Absorption Spectroscopy. *Structural Dynamics* **2017**, *4*, 044029, DOI: `10.1063/1.4985056`.

(27) Kaplan, C. J.; Kraus, P. M.; Ross, A. D.; Zürch, M.; Cushing, S. K.; Jager, M. F.; Chang, H.-T.; Gullikson, E. M.; Neumark, D. M.; Leone, S. R. Femtosecond Tracking of Carrier Relaxation in Germanium with Extreme Ultraviolet Transient Reflectivity. *Physical Review B* **2018**, *97*, 1716–1720, DOI: `10.1103/PhysRevB.97.205202`.

(28) Liu, H.; Michelsen, J. M.; Mendes, J. L.; Klein, I. M.; Bauers, S. R.; Evans, J. M.; Zakutayev, A.; Cushing, S. K. Measuring Photoexcited Electron and Hole Dynamics in ZnTe and Modeling Excited State Core-Valence Effects in Transient Extreme Ultraviolet Reflection Spectroscopy. *The Journal of*

Physical Chemistry Letters **2023**, *14*, 2106–2111, DOI: `10.1021/acs.jpclett.2c03894`.

(29) Cushing, S. K.; Zürch, M.; Kraus, P. M.; Carneiro, L. M.; Lee, A.; Chang, H.-T.; Kaplan, C. J.; Leone, S. R. Hot Phonon and Carrier Relaxation in Si(100) Determined by Transient Extreme Ultraviolet Spectroscopy. *Structural Dynamics* **2018**, *5*, 054302, DOI: `10.1063/1.5038015`.

(30) Bressler, C.; Chergui, M. Ultrafast X-ray Absorption Spectroscopy. *Chemical Reviews* **2004**, *104*, 1781–1812, DOI: `10.1021/cr0206667`.

(31) Bergmann, U.; Kern, J.; Schoenlein, R. W.; Wernet, P.; Yachandra, V. K.; Yano, J. Using X-ray Free-Electron Lasers for Spectroscopy of Molecular Catalysts and Metalloenzymes. *Nature Reviews Physics* **2021**, *3*, 264–282, DOI: `10.1038/s42254-021-00289-3`.

(32) Auböck, G.; Chergui, M. Sub-50-Fs Photoinduced Spin Crossover in [Fe(bpy)$_3$]$^{2+}$. *Nature Chemistry* **2015**, *7*, 629–633.

(33) Thomas, A.; Lethuillier-Karl, L.; Nagarajan, K.; Vergauwe, R. M. A.; George, J.; Chervy, T.; Shalabney, A.; Devaux, E.; Genet, C.; Moran, J.; Ebbesen, T. W. Tilting a Ground-State Reactivity Landscape by Vibrational Strong Coupling. *Science* **2019**, *363*, 615–619, DOI: `10.1126/science.aau7742`.

(34) Campos-Gonzalez-Angulo, J. A.; Ribeiro, R. F.; Yuen-Zhou, J. Resonant Catalysis of Thermally Activated Chemical Reactions with Vibrational Polaritons. *Nature Communications* **2019**, *10*, 4685, DOI: `10.1038/s41467-019-12636-1`.

(35) Fleming, G. R., *Chemical Applications of Ultrafast Spectroscopy*; Oxford University Press: 1986.

(36) Biswas, S.; Wallentine, S.; Bandaranayake, S.; Baker, L. R. Controlling Polaron Formation at Hematite Surfaces by Molecular Functionalization Probed by XUV Reflection-Absorption Spectroscopy. *The Journal of Chemical Physics* **2019**, *151*, 104701, DOI: `10.1063/1.5115163`.

(37) Bostedt, C.; Boutet, S.; Fritz, D. M.; Huang, Z.; Lee, H. J.; Lemke, H. T.; Robert, A.; Schlotter, W. F.; Turner, J. J.; Williams, G. J. Linac Coherent Light Source: The First Five Years. *Reviews of Modern Physics* **2016**, *88*, 015007, DOI: `10.1103/RevModPhys.88.015007`.

(38) Pellegrini, C.; Marinelli, A.; Reiche, S. The Physics of X-ray Free-Electron Lasers. *Reviews of Modern Physics* **2016**, *88*, 015006, DOI: `10.1103/RevModPhys.88.015006`.

(39) Popmintchev, T. et al. Bright Coherent Ultrahigh Harmonics in the keV X-ray Regime from Mid-Infrared Femtosecond Lasers. *Science* **2012**, *336*, 1287–1291, DOI: `10.1126/science.1218497`.

(40) Lewenstein, M.; Balcou, P.; Ivanov, M.; L'Huillier, A.; Corkum, P. Theory of High-Harmonic Generation by Low-Frequency Laser Fields. *Physical Review A: Atomic, Molecular, and Optical Physics* **1994**, *49*, 2117–2132.

(41) Krausz, F.; Ivanov, M. Attosecond Physics. *Reviews of Modern Physics* **2009**, *81*, 163–234, DOI: `10.1103/RevModPhys.81.163`.

(42) Brabec, T.; Krausz, F. Intense Few-Cycle Laser Fields: Frontiers of Nonlinear Optics. *Reviews of Modern Physics* **2000**, *72*, 545–591, DOI: `10.1103/RevModPhys.72.545`.

(43) Hergott, J.-F.; Kovacev, M.; Merdji, H.; Hubert, C.; Mairesse, Y.; Jean, E.; Breger, P.; Agostini, P.; Carré, B.; Salières, P. Extreme-Ultraviolet High-Order Harmonic Pulses in the Microjoule Range. *Physical Review A: Atomic, Molecular, and Optical Physics* **2002**, *66*, 021801.

(44) Koralek, J. D.; Kim, J. B.; Brůža, P.; Curry, C. B.; Chen, Z.; Bechtel, H. A.; Cordones, A. A.; Sperling, P.; Toleikis, S.; Kern, J. F.; Moeller, S. P.; Glenzer, S. H.; DePonte, D. P. Generation and Characterization of Ultrathin Free-Flowing Liquid Sheets. *Nature Communications* **2018**, *9*, 1353, DOI: `10.1038/s41467-018-03696-w`.

(45) Ekimova, M.; Quevedo, W.; Faubel, M.; Wernet, P.; Nibbering, E. A Liquid Flatjet System for Solution Phase Soft-X-ray Spectroscopy. *Structural Dynamics* **2015**, *2*, 054301.

(46) Luu, T. T.; Yin, Z.; Jain, A.; Gaumnitz, T.; Pertot, Y.; Ma, J.; Wörner, H. J. Extreme–Ultraviolet High–Harmonic Generation in Liquids. *Nature Communications* **2018**, *9*, 3723, DOI: `10.1038/s41467-018-06040-4`.

(47) Smith, A. D.; Balčiunas, T.; Chang, Y.-P.; Schmidt, C.; Zinchenko, K.; Nunes, F. B.; Rossi, E.; Svoboda, V.; Yin, Z.; Wolf, J.-P.; Wörner, H. J. Femtosecond Soft-X-ray Absorption Spectroscopy of Liquids with a Water-Window High-Harmonic Source. *The Journal of Physical Chemistry Letters* **2020**, *11*, 1981–1988, DOI: `10.1021/acs.jpclett.9b03559`.

(48) Kato, K.; Mashiko, H.; Kunihashi, Y.; Omi, H.; Gotoh, H.; Oguri, K. Highly Sensitive Transient Reflection Measurement in Extreme Ultraviolet Region for Tracking Carrier and Coherent Phonon Dynamics. *Optics Express* **2020**, *28*, 1595, DOI: `10.1364/OE.381585`.

(49) Franchini, C.; Reticcioli, M.; Setvin, M.; Diebold, U. Polarons in Materials. *Nature Reviews Materials* **2021**, 1–27, DOI: `10.1038/s41578-021-00289-w`.

(50) Emin, D. Optical Properties of Large and Small Polarons and Bipolarons. *Physical Review B* **1993**, *48*, 13691–13702.

(51) Miyata, K.; Atallah, T. L.; Zhu, X.-Y. Lead Halide Perovskites: Crystal-liquid Duality, Phonon Glass Electron Crystals, and Large Polaron Formation. *Science Advances* **2017**, *3*, e1701469, DOI: `10.1126/sciadv.1701469`.

(52) Guzelturk, B.; Winkler, T.; Goor, T.; Smith, M.; Bourelle, S.; Feldmann, S.; Trigo, M.; Teitelbaum, S.; Steinrück, H.-G.; Pena, G. Visualization of Dynamic Polaronic Strain Fields in Hybrid Lead Halide Perovskites. *Nature Materials* **2021**, *20*, 618–623.

(53) Ziwritsch, M.; Müller, S.; Hempel, H.; Unold, T.; Abdi, F.; Krol, R.; Friedrich, D.; Eichberger, R. Direct Time-Resolved Observation of Carrier Trapping and Polaron Conductivity in $BiVO_4$. *ACS Energy Letters* **2016**, *1*, 888–894.

(54) Porter, I. J.; Cushing, S. K.; Carneiro, L. M.; Lee, A.; Ondry, J. C.; Dahl, J. C.; Chang, H.-T.; Alivisatos, A. P.; Leone, S. R. Photoexcited Small Polaron Formation in Goethite (α-FeOOH) Nanorods Probed by Transient Extreme Ultraviolet Spectroscopy. *The Journal of Physical Chemistry Letters* **2018**, *9*, 4120–4124, DOI: `10.1021/acs.jpclett.8b01525`.

(55) Géneaux, R.; Kaplan, C. J.; Yue, L.; Ross, A. D.; Bækhøj, J. E.; Kraus, P. M.; Chang, H.-T.; Guggenmos, A.; Huang, M.-Y.; Zürch, M.; Schafer, K. J.; Neumark, D. M.; Gaarde, M. B.; Leone, S. R. Attosecond Time-Domain Measurement of Core-Level-Exciton Decay in Magnesium Oxide. *Physical Review Letters* **2020**, *124*, 207401, DOI: `10.1103/PhysRevLett.124.207401`.

(56) Porter, I.; Lee, A.; Cushing, S.; Chang, H.-T.; Ondry, J.; Alivisatos, A.; Leone, S. Characterization of Carrier Cooling Bottleneck in Silicon Nanoparticles by Extreme Ultraviolet (XUV) Transient Absorption Spectroscopy. *Journal of Physical Chemistry C* **2021**.

(57) Nayak, P. K.; Mahesh, S.; Snaith, H. J.; Cahen, D. Photovoltaic Solar Cell Technologies: Analysing the State of the Art. *Nature Reviews Materials* **2019**, *4*, 269–285, DOI: `10.1038/s41578-019-0097-0`.

(58) Tagliabue, G.; DuChene, J. S.; Abdellah, M.; Habib, A.; Gosztola, D. J.; Hattori, Y.; Cheng, W.-H.; Zheng, K.; Canton, S. E.; Sundararaman, R.; Sá, J.; Atwater, H. A. Ultrafast Hot-Hole Injection Modifies Hot-Electron Dynamics in Au/p-GaN Heterostructures. *Nature Materials* **2020**, *19*, 1312–1318, DOI: `10.1038/s41563-020-0737-1`.

(59) Dorkel, J. M.; Leturcq, P. Carrier Mobilities in Silicon Semi-Empirically Related to Temperature, Doping and Injection Level. *Solid-State Electronics* **1981**, *24*, 821–825, DOI: `10.1016/0038-1101(81)90097-6`.

(60) Marsh, B. M.; Lamoureux, B. R.; Leone, S. R. Ultrafast Time-Resolved Extreme Ultraviolet (XUV) Photoelectron Spectroscopy of Hole Transfer in a Zn/n-GaP Schottky Junction. *Structural Dynamics* **2018**, *5*, 054502, DOI: `10.1063/1.5046776`.

(61) Chang, H.-T.; Guggenmos, A.; Cushing, S.; Cui, Y.; Din, N.; Acharya, S.; Porter, I.; Kleineberg, U.; Turkowski, V.; Rahman, T. Electron Thermalization and Relaxation in Laser-Heated Nickel by Few-Femtosecond Core-Level Transient Absorption Spectroscopy. *Physical Review B* **2021**, *103*, 064305.

(62) Brown, M.; Peierls, R.; Stern, E. White Lines in X-ray Absorption. *Physical Review B* **1977**, *15*, 738–744.

(63) Stavitski, E.; De Groot, F. M. The CTM4XAS Program for EELS and XAS Spectral Shape Analysis of Transition Metal L Edges. *Micron* **2010**, *41*, 687–694, DOI: `10.1016/j.micron.2010.06.005`.

(64) Bruner, A.; Hernandez, S.; Mauger, F.; Abanador, P. M.; LaMaster, D. J.; Gaarde, M. B.; Schafer, K. J.; Lopata, K. Attosecond Charge Migration with TDDFT: Accurate Dynamics from a Well-Defined Initial State. *The Journal of Physical Chemistry Letters* **2017**, *8*, 3991–3996, DOI: `10.1021/acs.jpclett.7b01652`.

(65) Lee, S. H.; Lin, J. C.; Farmand, M.; Landers, A. T.; Feaster, J. T.; Avilés Acosta, J. E.; Beeman, J. W.; Ye, Y.; Yano, J.; Mehta, A.; Davis, R. C.; Jaramillo, T. F.; Hahn, C.; Drisdell, W. S. Oxidation State and Surface Reconstruction of Cu under CO_2 Reduction Conditions from *In Situ* X-ray Characterization. *Journal of the American Chemical Society* **2021**, *143*, 588–592, DOI: `10.1021/jacs.0c10017`.

(66) Helk, T.; Berger, E.; Jamnuch, S.; Hoffmann, L.; Kabacinski, A.; Gautier, J.; Tissandier, F.; Goddet, J.-P.; Chang, H.-T.; Oh, J.; Pemmaraju, C. D.; Pascal, T. A.; Sebban, S.; Spielmann, C.; Zuerch, M. Table-Top Extreme Ultraviolet Second Harmonic Generation. *Science Advances* **2021**, *7*, eabe2265, DOI: `10.1126/sciadv.abe2265`.

(67) Rouxel, J. R. et al. Hard X-ray Transient Grating Spectroscopy on Bismuth Germanate. *Nature Photonics* **2021**, 1–5, DOI: `10.1038/s41566-021-00797-9`.

(68) Schoenlein, R.; Elsaesser, T.; Holldack, K.; Huang, Z.; Kapteyn, H.; Murnane, M.; Woerner, M. Recent Advances in Ultrafast X-ray Sources. *Philosophical Transactions of the Royal Society A: Mathematical, Physical and Engineering Sciences* **2019**, *377*, 20180384, DOI: `10.1098/rsta.2018.0384`.

(69) Glover, T. E. et al. X-ray and Optical Wave Mixing. *Nature* **2012**, *488*, 603–608, DOI: `10.1038/nature11340`.

(70) Tamasaku, K.; Sawada, K.; Nishibori, E.; Ishikawa, T. Visualizing the Local Optical Response to Extreme-Ultraviolet Radiation with a Resolution of λ/380. *Nature Physics* **2011**, *7*, 705–708, DOI: `10.1038/nphys2044`.

(71) Higley, D. J. et al. Femtosecond X-ray Magnetic Circular Dichroism Absorption Spectroscopy at an X-ray Free Electron Laser. *Review of Scientific Instruments* **2016**, *87*, 033110, DOI: `10.1063/1.4944410`.

(72) Kfir, O.; Grychtol, P.; Turgut, E.; Knut, R.; Zusin, D.; Popmintchev, D.; Popmintchev, T.; Nembach, H.; Shaw, J. M.; Fleischer, A.; Kapteyn, H.; Murnane, M.; Cohen, O. Generation of Bright Phase-Matched Circularly-Polarized Extreme Ultraviolet High Harmonics. *Nature Photonics* **2015**, *9*, 99–105, DOI: `10.1038/nphoton.2014.293`.

Chapter 3

MEASURING PHOTOEXCITED ELECTRON AND HOLE DYNAMICS IN ZNTE AND MODELING EXCITED STATE CORE-VALENCE EFFECTS IN TRANSIENT EXTREME ULTRAVIOLET REFLECTION SPECTROSCOPY

Photoelectrochemical CO_2 conversion requires efficient photoabsorbers and catalysts to generate and transport charge carriers to synthesize value-added products. This chapter discusses measurements of carrier and structural dynamics in the wide band gap semiconductor zinc telluride (ZnTe). ZnTe and related II-VI compounds (e.g. $ZnTe_xSe_{1-x}$) are attractive light-absorber candidates for driving the CO_2 reduction reaction. Using transient XUV reflection spectroscopy, we simultaneously measure femtosecond non-equilibrium electron and hole dynamics at the material's surface. The carrier-specific measurement enables the direct understanding of each charge carrier's relaxation, diffusion, and recombination kinetics. Further, the chapter introduces an integrated theory framework for incorporating excited state effects into the Bethe-Salpeter equation approach, accurately modeling experimental spectra from first principles.

This chapter is adapted with permission from

3.1 Abstract

Transient extreme ultraviolet (XUV) spectroscopy is becoming a valuable tool for characterizing solar energy materials because it can separate photoexcited electron and hole dynamics wiwth element-specificity. Here, we use surface-sensitive femtosecond XUV reflection spectroscopy to separately measure photoexcited electron, hole, and band gap dynamics of ZnTe, a promising photocathode for CO_2 reduction. We develop an ab initio theoretical framework based on density functional theory and the Bethe-Salpeter equation to robustly assign the complex transient XUV spectra to the material's electronic states. Applying this framework, we identify the relaxation pathways and quantify their timescales in photoexcited ZnTe, including sub-picosecond hot electron and hole thermalization, surface carrier diffusion, ultrafast band gap renormalization, and evidence of acoustic phonon oscillations.

3.2 Introduction

Photoelectrochemical reduction and oxidation reactions are driven by the charge transfer of electrons or holes at an electrode's surface.[1–3] Thus, it is necessary to develop surface-sensitive experimental probes that can separate photoexcited electron and hole kinetics. Knowing the initial excess energy of hot electrons and holes, their thermalization time, and charge transfer pathways is crucial for optimizing photoelectrochemical reactions and devices.[4, 5] For example, hot carriers with excess kinetic energy have been proposed for steering selectivity in photocatalysis.[6] Characterizing the carrier-specific ultrafast photodynamics in II-VI semiconductors is desirable due to their application in photoelectrodes,[7–10] as well as in optoelectronics,[11] electro-optical detectors,[12] and photovoltaics.[13, 14] Recently, ZnTe has gained attention as a photocathode material for CO_2 reduction due to its aqueous stability at reducing conditions and its conduction band edge energy position, which facilitates electron transfer to the reaction species.[15] To truly understand the microscopic mechanisms governing the performance of such photoelectrochemical systems, it is necessary to first understand the photodynamics of the light absorber by isolating the underlying electron and hole energetics, surface carrier kinetics including diffusion and recombination, as well as any associated structural dynamics.[16]

Transient extreme ultraviolet (XUV) spectroscopy measures ultrafast element- and carrier-specific dynamics by exciting a core-level electron into valence states.[17–20] XUV spectroscopy in a grazing-angle reflection geometry offers high surface sensitivity because of the low penetration depth (1-10 nm) of the photons in solids.[21]

In addition to carrier dynamics, structural dynamics at the surface can also be measured.[22] However, the complexity and richness of the transient XUV spectra of solid-state materials presents challenges for extracting the underlying photodynamics. For example, experimental spectra often contain mixed electronic-structural dynamics because of the shallow energy core-hole perturbation from the XUV probe transition. Due to the core-hole perturbation, the XUV absorption or reflection spectrum usually does not directly map out the unperturbed band structure and carrier occupation of interest.[19, 22–26]The extent to which the density of states is modified depends on the valence electronic configuration of the material. For instance, for some semiconductors, electrons and holes can be directly resolved from the experiment and global fit of transient XUV spectra.[17, 18, 27] However, directly extracting carrier kinetics is not possible for most materials, such as transition metal compounds with highly localized 3d orbitals where angular momentum coupling changes the XUV spectral shape compared to the unoccupied density of states.[24, 28–30] Here, in addition to experimental results, we present a unified, ab initio theoretical framework for modeling excited state XUV and X-ray spectra that can be applied to a range of materials at different absorption edges. The theoretical methods are especially necessary when performing transient XUV spectroscopy in a reflection geometry, where changes in both the real and imaginary parts of the refractive index must be considered.[31, 32]

In this study, we use transient XUV reflection spectroscopy to measure the ultrafast electron and hole dynamics at the surface of ZnTe. Experimentally, transient XUV reflection spectra are measured at the Te $N_{4,5}$ edges ($4d_{3/2, 5/2}$ core states) around 40 eV following photoexcitation with a ~50 fs, 3.1 eV (400 nm) pulse. The XUV probe pulse has a sample penetration depth of ~2 nm at a 10° grazing incidence angle. We measure a hot electron thermalization time of 330 ± 100 fs and a hot hole thermalization time of 340 ± 320 fs. Using our modified Bethe-Salpeter equation approach, the hot carrier thermalization pathways can be mapped back onto the band structure. The electron and hole diffusion times are determined to be 2.21 ± 1.12 ps for electrons and 3.91 ± 3.58 ps for holes. In addition to carrier dynamics, we also measure an initial photoexcited band gap renormalization with a decay time of 730 ± 170 fs. Evidence of surface acoustic phonons is also measured as intensity oscillations in the spectra. More broadly, this paper demonstrates an ab initio approach to interpret transient XUV measurements without the need for system-specific approximate models.[22, 33] This approach is also applicable to higher energy X-ray edges measured at free electron lasers and synchrotrons.
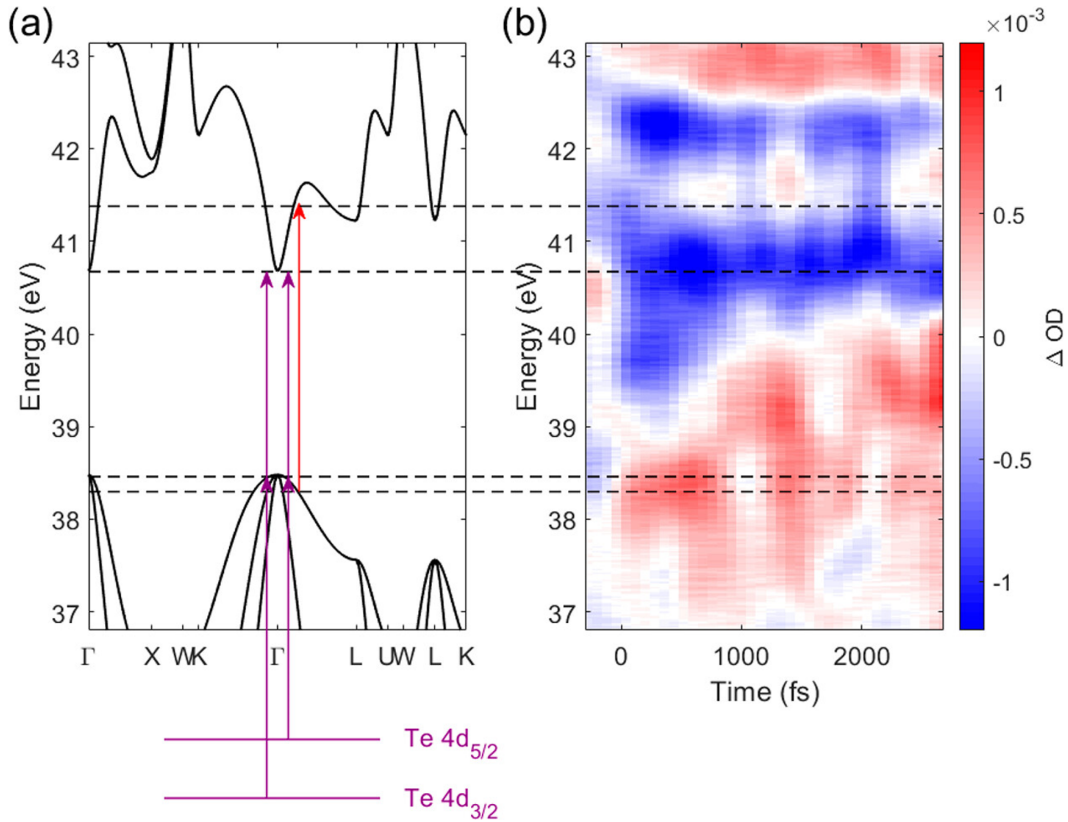
Figure 3.1: (a) The calculated band structure of ZnTe is overlaid with optical photoexcitation and core-to-valence XUV probe transitions. The red arrow indicates a 3.1 eV (400 nm) optical excitation between the valence and conduction bands. Core-to-valence probe transitions are labeled with purple arrows. (b) Measured transient XUV reflection-absorption near the Te $N_{4,5}$ edges after photoexcitation. The main transient features due to state filling include a decrease in absorption (increase in reflection) between 40.75 eV and 42.25 eV (blue features). An increase in absorption (decrease in reflection) is measured starting at 38 eV and broadens to 39.5 eV approximately 1 ps after optical excitation (red features). Additionally, in-gap dynamics are observed, showing an initial decrease in absorption below 40 eV, which blue shifts and disappears over time. The alignment of the transient spectral features to the valence and conduction band are indicated by the dashed lines.

As shown in Figure 3.1(a), optical excitation at 3.1 eV (400 nm) promotes electrons to the otherwise empty conduction bands of ZnTe, blocking allowed XUV transitions to the same states in the transient spectrum. On the other hand, the creation of photoexcited holes allows new core electron transitions to the valence band. The change in the transient reflection after optical excitation is defined using Equation 3.1:

$$\Delta OD = -\log_{10}\left(\frac{I_{pump\ on}}{I_{pump\ off}}\right) \tag{3.1}$$

This definition is often termed reflection-absorption, due to the negative sign in Equation 3.1.[34] The measured transient XUV reflection spectra around the Te $N_{4,5}$ absorption edges are shown in Figure 3.1(b) for an excitation density of 1.74 mJ/cm^2. The blue color is a decrease in absorption (increased reflectivity) while the red color is an increase in absorption (decreased reflectivity). After photoexcitation, two dominant decreased absorption features (blue) are measured centered at 40.75 eV and 42.25 eV along with a dominant increased absorption (red) below 40 eV. The probed Te $N_{4,5}$ absorption edges involve XUV transitions from two core states, $4d_{3/2}$ and $4d_{5/2}$, separated by ~1.6 eV. The decreased absorption (blue) at 40.75 eV and 42.25 eV correspond to XUV transitions from $4d_{5/2,\,3/2}$ core levels to the conduction bands. In general, photoexcited electrons in the conduction bands will block core-to-conduction band transitions. Similarly, the photoexcited holes lead to increased absorption (red) below 40 eV.

To robustly assign the electron and hole dynamics, a combined density functional theory (DFT) and Bethe-Salpeter Equation (BSE) approach is used to model the core-valence transitions that compose the measured XUV peaks. First, ground state XUV reflection spectra are calculated using Quantum ESPRESSO and the Obtaining Core-level Excitations using Ab initio calculations and the NIST BSE solver (OCEAN) code (Supporting Information Figure A.10).[28, 29, 35] The band gap obtained from the DFT calculation is corrected using a scissor correction to match the experimentally observed band gap. To capture the effects of photoexcited electrons and holes on the XUV spectra, the standard code is modified using an adiabatic approximation to the core-level excited states since the lifetime of the core-level exciton (attoseconds) is shorter than the measured photoexcited valence dynamics (femtoseconds and longer). To simulate the excited state valence dynamics, the carrier occupation in the conduction or valence bands are changed at different k-points in momentum space. Various electron and hole state filling configurations are calculated to cover possible photoexcitation and thermalization pathways based on the optical pump energy and the material's band structure. The calculation results are then independently fitted to experimental data at each pump-probe time delay to extract the carrier distribution.

In Figure 3.2(a), the theoretical spectra accurately reproduce the experimental measurements. A comparison is shown between the calculated XUV spectra (dashed lines) with the measured transient XUV reflection spectra (solid lines). Spectral lineouts are shown for the initial photoexcited states (blue lines) and the steady-
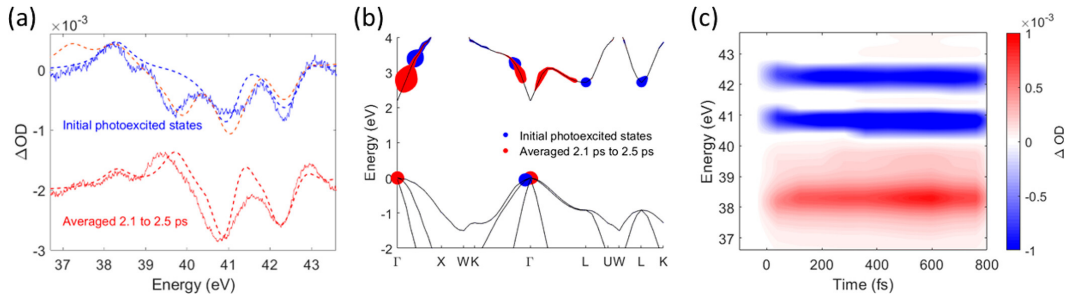
Figure 3.2: (a) Comparison of experimental (solid lines) and theoretical spectra (dashed lines) for initial photoexcited carrier states (blue lines) and fully thermalized final states (red lines). Calculated transient XUV reflection are plotted as dashed lines, reproducing the main carrier-specific experimental spectral signatures. For the thermalized final states, modeled state filling effects (red dashed line) accurately reproduce the experimental features (red solid line). For the initial non-equilibrium photoexcited states, an additional mid-gap feature is measured, which is not reproduced by modeling state filling effects (blue dashed line). A more accurate fit to the experiment is achieved by approximating the mid-gap feature as pump-induced transitions to mid-gap states (orange dashed line), which is consistent with band gap renormalization or defect states. (b) From matching the experimental spectra to the theoretical calculations, approximate time-dependent carrier occupations can be inferred in momentum space. Differential momentum-resolved XUV transition amplitudes are shown for the theoretical state filling conditions that match experimental spectra in (a). The XUV transition amplitude reflects the underlying photoexcited carrier distribution. (c) The approximate time-dependent carrier occupations are used to model the spectral contributions from state filling effects, matching the measured experimental carrier thermalization in Figure 3.1(b). The reconstruction is performed for the first 800 fs after photoexcitation, when hot carrier relaxation has largely finished and before phonon-induced intensity modulations dominate the spectrum.

state signal when carriers are fully thermalized (red lines), averaged over 2.1 ps to 2.5 ps to remove the effect of phonon-induced intensity oscillations. Due to the energy splitting of Te $4d_{3/2}$ and $4d_{5/2}$ core states, there are duplicate spectral features from core-to-valence transitions originating from different initial core states. For the final thermalized states, modeling based on state filling effects (dashed red line) is in excellent agreement with the experimental spectra (solid red line). For the initial photoexcited states, theoretical spectra are calculated for state filling effects only (blue dashed line) and state filling effects combined with transitions to mid-gap states (orange dashed line). Better agreement with experiment is achieved by including these mid-gap transitions, which represent a smaller band gap transition that would result from band gap renormalization or defect states. Once the

theoretical and experimental spectra are matched, the corresponding XUV transitions in momentum space can be extracted as shown in Figure 3.2(b), reflecting the modeled photoexcited electron and hole distribution in the conduction and valence bands. The non-equilibrium electron and hole thermalization becomes apparent in the reconstructed spectra (Figure 3.2(c)).

The mid-gap feature is assigned to band gap renormalization based on the material's low defect density and the transient signal's dependence on excitation fluence. Band gap renormalization is a many-body effect where the photoexcited electrons and holes have a Coulomb attraction which decreases the band gap.[36] In principle, both mid-gap defects and many-body band gap renormalization could account for the mid-gap feature that is not reproduced by state-filling effects (Figure 3.2(a)). If the experimental spectrum was interpreted without theory, the origin of the mid-gap feature would seem to be associated with mid-gap defect states based on its energy alignment relative to the conduction and valence bands. In order for defect states to be responsible for the mid-gap feature, the defect density would need to be on the order of the photoexcited carrier density ($>10^{18}$ carriers/cm^3) since the intensity of the mid-gap feature is similar to that of the state filling features. However, XPS and 4-point probe measurements do not reveal any defect levels above 5×10^8 cm^{-3} (Supporting Information Section A.1). Additionally, no mid-gap states were measured using ground state optical absorption (Figure A.6, A.7). Similar band gap dynamics were measured in ZnTe thin film samples by different growth methods (Figure A.12), which indicates that the feature is intrinsic to ZnTe and is not related to defect states. Measurements at different optical excitation fluences exhibit a larger band shift energy and longer recovery lifetime (Figure A.12(b)), consistent with band gap renormalization.

While fundamentally the theoretical DFT+BSE approach is a frequency-domain method, this back-extraction process provides an approximate understanding of the carrier evolution in momentum space after photoexcitation. Ultimately, the theoretical resolution is limited by the number of sampling positions in momentum space used in the DFT calculation and the intrinsic experimental spectral fluctuations. While our theoretical approach provides an estimate of the carrier distribution in momentum space, it must be stressed that this is an approximation as the measured XUV spectra is summed over all dipole allowed transitions. As a result, estimating the momentum-resolved carrier distribution will work best for materials exhibiting few highly dispersive bands near the optical transitions. A detailed discussion of

this method, including its resolution and limitations, can be found in the Supporting Information Section A5.2. After robust assignment using the DFT+BSE theoretical
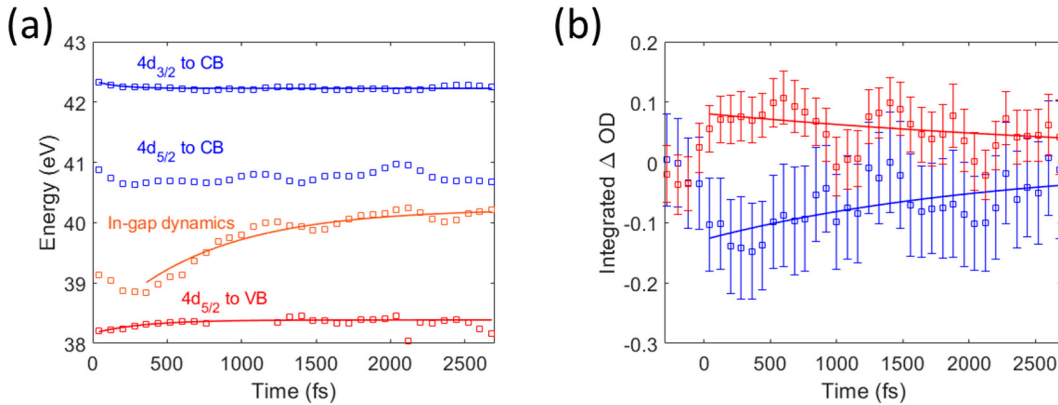

Figure 3.3: (a) Extracted electron, hole, and band gap renormalization dynamics from the experimental spectra using the DFT+BSE approach. An exponential fit of the electron feature for the Te $4d_{3/2}$ to conduction band transition in the first 920 fs reveals an electron thermalization time of 330 ± 100 fs. An exponential fit of the hole feature in the first 760 fs yields a hole thermalization time of 340 ± 320 fs. These fitting ranges are chosen before the intensity modulation from the acoustic phonons dominates the spectra. The band gap renormalization dynamics are extracted by tracing the energy shift of the spectral zero-crossing for the $4d_{5/2}$ to conduction band transition, and are found to have a time constant of 730 ± 170 fs. (b) The spectral intensity for electrons (blue) are integrated between 41.75 eV to 42.56 eV while the spectral intensity for holes (red) are integrated between 37.88 eV to 38.75 eV. Exponential fits give diffusion time constants of 2.21 ± 1.12 ps and 3.91 ± 3.58 ps for electrons and holes, respectively.

framework, the electron and hole kinetics are extracted from the experiment (Figure 3.3(a)). The electronic $4d_{5/2}$ to conduction band transition is modulated by the nearby hole feature from the $4d_{3/2}$ to valence band transition. Due to this spectral overlap, electron kinetics are extracted using the $4d_{3/2}$ to conduction band transition, while hole kinetics are extracted using the $4d_{5/2}$ to valence band transition. The thermalization times are found to be 330 ± 100 fs for electrons and 340 ± 320 fs for holes using an exponential fit. Evidence of phonon oscillations is also observed, with a frequency of 2.79 THz (93 cm^{-1}), matching the acoustic phonon dispersion branches around the Γ point (Figure A.12(b), A.13).[37]

While carrier kinetics are extracted from spectral shifts, the intensity of the photoexcited spectrum corresponds to the diffusion of the photoexcited carriers away from the sample surface. As shown in Figure 3.3(b), the carrier populations decrease with a time constant of 2.21 ± 1.12 ps for electrons and 3.91 ± 3.58 ps for

holes. This decay in transient signal is assigned to carrier diffusion rather than recombination since a nanosecond measurement reveals no change in intensity after the first few picoseconds, suggesting a carrier lifetime of greater than 1 ns (Figure A.14). Due to the weak signal of the carrier diffusion, the time constants feature large confidence intervals, motivating future measurements to fully quantify this surface carrier diffusion effect.

3.3 Conclusion

This paper demonstrates using femtosecond XUV reflection spectroscopy and ab initio theory to extract surface non-equilibrium electron, hole, and band gap dynamics as well as the carrier diffusion times at the surface of ZnTe. These carrier-specific dynamics are critical for understanding photoelectrochemical reactions and other renewable energy applications, where transient X-ray measurements are moving towards in-situ environments.[38, 39] The necessity of an ab initio predictive framework to robustly assign spectral features in solids is stressed. As an example, the carrier kinetics in this work are experimentally obscured by a mid-band gap feature. In a broader context of method development, our theoretical approach allows the robust interpretation of transient XUV and X-ray spectra without the use of semi-empirical, material-dependent parameters.

References

(1) Gray, H. B. Powering the Planet with Solar Fuel. *Nature Chemistry* **2009**, *1*, 7, DOI: 10.1038/nchem.141.

(2) Tran, P. D.; Wong, L. H.; Barber, J.; Loo, J. S. C. Recent Advances in Hybrid Photocatalysts for Solar Fuel Production. *Energy & Environmental Science* **2012**, *5*, 5902–5818, DOI: 10.1039/c2ee02849b.

(3) Li, J.; Wu, N. Semiconductor-Based Photocatalysts and Photoelectrochemical Cells for Solar Fuel Generation: A Review. *Catalysis Science & Technology* **2015**, *5*, 1360–1384, DOI: 10.1039/C4CY00974F.

(4) De Nijs, B.; Benz, F.; Barrow, S. J.; Sigle, D. O.; Chikkaraddy, R.; Palma, A.; Carnegie, C.; Kamp, M.; Sundararaman, R.; Narang, P.; Scherman, O. A.; Baumberg, J. J. Plasmonic Tunnel Junctions for Single-Molecule Redox Chemistry. *Nature Communications* **2017**, *8*, 994, DOI: 10.1038/s41467-017-00819-7.

(5) Laskowski, F. A. L.; Oener, S. Z.; Nellist, M. R.; Gordon, A. M.; Bain, D. C.; Fehrs, J. L.; Boettcher, S. W. Nanoscale Semiconductor/Catalyst Interfaces in Photoelectrochemistry. *Nature Materials* **2020**, *19*, 69–76, DOI: 10.1038/s41563-019-0488-z.

(6) Zhou, L.; Swearer, D. F.; Zhang, C.; Robatjazi, H.; Zhao, H.; Henderson, L.; Dong, L.; Christopher, P.; Carter, E. A.; Nordlander, P.; Halas, N. J. Quantifying Hot Carrier and Thermal Contributions in Plasmonic Photocatalysis. *Science* **2018**, *362*, 69–72, DOI: `10.1126/science.aat6967`.

(7) Won, D. H.; Chung, J.; Park, S. H.; Kim, E.-H.; Woo, S. I. Photoelectrochemical Production of Useful Fuels from Carbon Dioxide on a Polypyrrole-Coated p-ZnTe Photocathode under Visible Light Irradiation. *Journal of Materials Chemistry A* **2015**, *3*, 1089–1095, DOI: `10.1039/C4TA05901H`.

(8) Jang, Y. J.; Jang, J.-W.; Lee, J.; Kim, J. H.; Kumagai, H.; Lee, J.; Minegishi, T.; Kubota, J.; Domen, K.; Lee, J. S. Selective CO Production by Au Coupled ZnTe/ZnO in the Photoelectrochemical CO_2 Reduction System. *Energy & Environmental Science* **2015**, *8*, 3597–3604, DOI: `10.1039/C5EE01445J`.

(9) Jang, Y. J.; Jeong, I.; Lee, J.; Lee, J.; Ko, M. J.; Lee, J. S. Unbiased Sunlight-Driven Artificial Photosynthesis of Carbon Monoxide from CO_2 Using a ZnTe-Based Photocathode and a Perovskite Solar Cell in Tandem. *ACS Nano* **2016**, *10*, 6980–6987, DOI: `10.1021/acsnano.6b02965`.

(10) Wang, Q.; Wang, X.; Yu, Z.; Jiang, X.; Chen, J.; Tao, L.; Wang, M.; Shen, Y. Artificial Photosynthesis of Ethanol Using Type-II g-C_3N_4/ZnTe Heterojunction in Photoelectrochemical CO_2 Reduction System. *Nano Energy* **2019**, *60*, 827–835, DOI: `10.1016/j.nanoen.2019.04.037`.

(11) Hazarika, A.; Fedin, I.; Hong, L.; Guo, J.; Srivastava, V.; Cho, W.; Coropceanu, I.; Portner, J.; Diroll, B. T.; Philbin, J. P.; Rabani, E.; Klie, R.; Talapin, D. V. Colloidal Atomic Layer Deposition with Stationary Reactant Phases Enables Precise Synthesis of "Digital" II–VI Nano-heterostructures with Exquisite Control of Confinement and Strain. *Journal of the American Chemical Society* **2019**, *141*, 13487–13496, DOI: `10.1021/jacs.9b04866`.

(12) Winnewisser, C.; Jepsen, P. U.; Schall, M.; Schyja, V.; Helm, H. Electro-Optic Detection of THz Radiation in $LiTaO_3$, $LiNbO_3$ and ZnTe. *Applied Physics Letters* **1997**, *70*, 3069–3071, DOI: `10.1063/1.119093`.

(13) Tanaka, T.; Miyabara, M.; Nagao, Y.; Saito, K.; Guo, Q.; Nishio, M.; Yu, K. M.; Walukiewicz, W. Photocurrent Induced by Two-Photon Excitation in ZnTeO Intermediate Band Solar Cells. *Applied Physics Letters* **2013**, *102*, 052111, DOI: `10.1063/1.4790643`.

(14) Garland, J. W.; Biegala, T.; Carmody, M.; Gilmore, C.; Sivananthan, S. Next-Generation Multijunction Solar Cells: The Promise of II-VI Materials. *Journal of Applied Physics* **2011**, *109*, 102423, DOI: `10.1063/1.3582902`.

(15) Singh, A. K.; Montoya, J. H.; Gregoire, J. M.; Persson, K. A. Robust and Synthesizable Photocatalysts for CO_2 Reduction: A Data-Driven Materials Discovery. *Nature Communications* **2019**, *10*, 443, DOI: `10.1038/s41467-019-08356-1`.

(16) Doherty, T. A. S. et al. Performance-Limiting Nanoscale Trap Clusters at Grain Junctions in Halide Perovskites. *Nature* **2020**, *580*, 360–366, DOI: `10.1038/s41586-020-2184-1`.

(17) Zürch, M.; Chang, H.-T.; Borja, L. J.; Kraus, P. M.; Cushing, S. K.; Gandman, A.; Kaplan, C. J.; Oh, M. H.; Prell, J. S.; Prendergast, D.; Pemmaraju, C. D.; Neumark, D. M.; Leone, S. R. Direct and Simultaneous Observation of Ultrafast Electron and Hole Dynamics in Germanium. *Nature Communications* **2017**, *8*, 15734, DOI: `10.1038/ncomms15734`.

(18) Attar, A. R.; Chang, H.-T.; Britz, A.; Zhang, X.; Lin, M.-F.; Krishnamoorthy, A.; Linker, T.; Fritz, D.; Neumark, D. M.; Kalia, R. K.; Nakano, A.; Ajayan, P.; Vashishta, P.; Bergmann, U.; Leone, S. R. Simultaneous Observation of Carrier-Specific Redistribution and Coherent Lattice Dynamics in 2H-MoTe$_2$ with Femtosecond Core-Level Spectroscopy. *ACS Nano* **2020**, *14*, 15829–15840, DOI: `10.1021/acsnano.0c06988`.

(19) Cushing, S. K.; Porter, I. J.; Roulet, B. R. de; Lee, A.; Marsh, B. M.; Szoke, S.; Vaida, M. E.; Leone, S. R. Layer-Resolved Ultrafast Extreme Ultraviolet Measurement of Hole Transport in a Ni-TiO$_2$-Si Photoanode. *Science Advances* **2020**, *6*, eaay6650, DOI: `10.1126/sciadv.aay6650`.

(20) Verkamp, M.; Leveillee, J.; Sharma, A.; Lin, M.-F.; Schleife, A.; Vura-Weis, J. Carrier-Specific Hot Phonon Bottleneck in CH$_3$NH$_3$PbI$_3$ Revealed by Femtosecond XUV Absorption. *Journal of the American Chemical Society* **2021**, *143*, 20176–20182, DOI: `10.1021/jacs.1c07817`.

(21) Cirri, A.; Husek, J.; Biswas, S.; Baker, L. R. Achieving Surface Sensitivity in Ultrafast XUV Spectroscopy: M$_{2,3}$-Edge Reflection–Absorption of Transition Metal Oxides. *The Journal of Physical Chemistry C* **2017**, *121*, 15861–15869, DOI: `10.1021/acs.jpcc.7b05127`.

(22) Cushing, S. K.; Zürch, M.; Kraus, P. M.; Carneiro, L. M.; Lee, A.; Chang, H.-T.; Kaplan, C. J.; Leone, S. R. Hot Phonon and Carrier Relaxation in Si(100) Determined by Transient Extreme Ultraviolet Spectroscopy. *Structural Dynamics* **2018**, *5*, 054302, DOI: `10.1063/1.5038015`.

(23) Carneiro, L. M.; Cushing, S. K.; Liu, C.; Su, Y.; Yang, P.; Alivisatos, A. P.; Leone, S. R. Excitation-Wavelength-Dependent Small Polaron Trapping of Photoexcited Carriers in α-Fe$_2$O$_3$. *Nature Materials* **2017**, *16*, 819–825, DOI: `10.1038/nmat4936`.

(24) De Groot, F. Multiplet Effects in X-ray Spectroscopy. *Coordination Chemistry Reviews* **2005**, *249*, 31–63.

(25) De Groot, F. High-Resolution X-ray Emission and X-ray Absorption Spectroscopy. *Chemical Reviews* **2001**, *101*, 1779–1808, DOI: `10.1021/cr9900681`.

(26) Liu, H.; Klein, I. M.; Michelsen, J. M.; Cushing, S. K. Element-Specific Electronic and Structural Dynamics Using Transient XUV and Soft X-ray Spectroscopy. *Chem* **2021**, *7*, 2569–2584, DOI: `10.1016/j.chempr.2021.09.005`.

(27) Kaplan, C. J.; Kraus, P. M.; Gullikson, E. M.; Borja, L. J.; Cushing, S. K.; Zürch, M.; Chang, H.-T.; Neumark, D. M.; Leone, S. R. Retrieval of the Complex-Valued Refractive Index of Germanium near the $M_{4,5}$ Absorption Edge. *Journal of the Optical Society of America B* **2019**, *36*, 1716, DOI: `10.1364/JOSAB.36.001716`.

(28) Vinson, J.; Rehr, J. J.; Kas, J. J.; Shirley, E. L. Bethe-Salpeter Equation Calculations of Core Excitation Spectra. *Physical Review B* **2011**, *83*, 115106, DOI: `10.1103/PhysRevB.83.115106`.

(29) Gilmore, K.; Vinson, J.; Shirley, E. L.; Prendergast, D.; Pemmaraju, C. D.; Kas, J. J.; Vila, F. D.; Rehr, J. J. Efficient Implementation of Core-Excitation Bethe–Salpeter Equation Calculations. *Computer Physics Communications* **2015**, *197*, 109–117, DOI: `10.1016/j.cpc.2015.08.014`.

(30) Klein, I. M.; Liu, H.; Nimlos, D.; Krotz, A.; Cushing, S. K. *Ab Initio* Prediction of Excited-State and Polaron Effects in Transient XUV Measurements of α-Fe_2O_3. *Journal of the American Chemical Society* **2022**, *144*, 12834–12841, DOI: `10.1021/jacs.2c03994`.

(31) Kaplan, C. J.; Kraus, P. M.; Ross, A. D.; Zürch, M.; Cushing, S. K.; Jager, M. F.; Chang, H.-T.; Gullikson, E. M.; Neumark, D. M.; Leone, S. R. Femtosecond Tracking of Carrier Relaxation in Germanium with Extreme Ultraviolet Transient Reflectivity. *Physical Review B* **2018**, *97*, 1716–1720, DOI: `10.1103/PhysRevB.97.205202`.

(32) Géneaux, R.; Timrov, I.; Kaplan, C. J.; Ross, A. D.; Kraus, P. M.; Leone, S. R. Coherent Energy Exchange between Carriers and Phonons in Peierls-distorted Bismuth Unveiled by Broadband XUV Pulses. *Physical Review Research* **2021**, *3*, 033210, DOI: `10.1103/PhysRevResearch.3.033210`.

(33) Cushing, S. K.; Lee, A.; Porter, I. J.; Carneiro, L. M.; Chang, H.-T.; Zürch, M.; Leone, S. R. Differentiating Photoexcited Carrier and Phonon Dynamics in the Δ, *L*, and Γ Valleys of Si(100) with Transient Extreme Ultraviolet Spectroscopy. *The Journal of Physical Chemistry C* **2019**, *123*, 3343–3352, DOI: `10.1021/acs.jpcc.8b10887`.

(34) Biswas, S.; Husek, J.; Baker, L. R. Elucidating Ultrafast Electron Dynamics at Surfaces Using Extreme Ultraviolet (XUV) Reflection–Absorption Spectroscopy. *Chemical Communications* **2018**, *54*, 4216–4230, DOI: `10.1039/C8CC01745J`.

(35) Giannozzi, P. et al. QUANTUM ESPRESSO: A Modular and Open-Source Software Project for Quantum Simulations of Materials. *Journal of Physics:*

Condensed Matter **2009**, *21*, 395502, DOI: `10.1088/0953-8984/21/39/395502`.

(36) Liu, F.; Ziffer, M. E.; Hansen, K. R.; Wang, J.; Zhu, X. Direct Determination of Band-Gap Renormalization in the Photoexcited Monolayer MoS$_2$. *Physical Review Letters* **2019**, *122*, 246803, DOI: `10.1103/PhysRevLett.122.246803`.

(37) Vagelatos, N.; Wehe, D.; King, J. S. Phonon Dispersion and Phonon Densities of States for ZnS and ZnTe. *The Journal of Chemical Physics* **1974**, *60*, 3613–3618, DOI: `10.1063/1.1681581`.

(38) Lee, S. H.; Lin, J. C.; Farmand, M.; Landers, A. T.; Feaster, J. T.; Avilés Acosta, J. E.; Beeman, J. W.; Ye, Y.; Yano, J.; Mehta, A.; Davis, R. C.; Jaramillo, T. F.; Hahn, C.; Drisdell, W. S. Oxidation State and Surface Reconstruction of Cu under CO$_2$ Reduction Conditions from *In Situ* X-ray Characterization. *Journal of the American Chemical Society* **2021**, *143*, 588–592, DOI: `10.1021/jacs.0c10017`.

(39) Bak, S.-M.; Shadike, Z.; Lin, R.; Yu, X.; Yang, X.-Q. In Situ/Operando Synchrotron-Based X-ray Techniques for Lithium-Ion Battery Research. *NPG Asia Materials* **2018**, *10*, 563–580, DOI: `10.1038/s41427-018-0056-z`.

C h a p t e r   4

DYNAMICAL POLARON DELOCALIZATION IN CUFEO$_2$ IMPROVES PHOTOEXCITED ELECTRON TRANSPORT

Ultrafast charge carrier self-trapping via polaron formation is pervasive in transition metal oxides. The formation of the polaron quasi-particle typically occurs on sub-picosecond timescales and limits charge transport on device timescales. This chapter investigates polaron formation in the photocathode copper iron oxide (CuFeO$_2$). Sub-picosecond small polaron formation after photoexcitation is measured in the form of charge transfer to the iron center and coherent lattice expansion between Fe-O layers. The comparison to photocathode iron oxide (α-Fe$_2$O$_3$) reveals improved carrier diffusion due to a polaron delocalization effect resulting from coherent lattice expansion between Fe-O layers and charge-sharing with surrounding Fe^{4+} atoms. This work offers insight into delocalization effects on polaron formation and provides methods for systematically measuring the carrier-structural dynamics behind polaron formation.

This chapter is adapted with permission from:

> Liu, H.; Mendes, J. L.; Michelsen, J. M.; Finn, B.; Cooper, J. K.; Cushing, S. K. Dynamical Polaron Delocalization in CuFeO$_2$ Improves Photoexcited Electron Transport. *In preparation*.

4.1 Abstract

Transition metal oxides have been widely studied for applications in photocatalysis. However, charge trapping via small polaron formation remains a significant bottleneck to realize efficient devices. Detailed measurements of small polaron dynamics have been performed. Yet, the relation of these small polaron dynamics to photoexcited transport is only inferred, rather than probed directly. Moreover, the mechanism of how small polarons couple to electronic states and lattice modes to control delocalization, and thus transport, remains unclear. Here, we characterize small polaron formation in $CuFeO_2$ using transient XUV reflection spectroscopy. We measure that adiabatic small polaron formation occurs on a ~100 fs timescale, similar to other Fe(III) compounds. Notably, following polaron formation, a dynamical delocalization of the small polaron occurs through a coherent lattice expansion between Fe-O layers and charge-sharing with surrounding Fe^{4+} states. Our work bridges atomic scale dynamics with mesoscale charge transport to provide a detailed, real-time observation of how electronic-structural coupling in a polaron-host material could be used to suppress polaronic effects for a variety of applications.

4.2 Introduction

Small polarons dominate transport in a variety of material physics spanning superconductivity, charge density waves, and transport in organic and inorganic materials.[1–6] The balance between strong electron correlations and strong electron-phonon coupling determines electronic properties from band gaps to charge transport.[4] For materials with photocatalytic applications, the effect of polaron dynamics on surface chemical kinetics that benefit from charge localization and lattice reorganization must also be considered.[7, 8] Iron oxide compounds, such as α-Fe_2O_3, are prototypical photocatalysts that have near-ideal charge-transfer-based band gaps and surface kinetics due to their localized d-orbitals. Yet, their photocatalytic efficiency is below the theoretical limit because the same localized orbitals lead to the formation of photoexcited, charge-transfer small polarons which reduce carrier mobility. While transition metal oxides that have an empty d-shell after bonding, such as TiO_2, tend to form photoexcited large polarons that have sufficient carrier mobilities to reach near theoretical efficiencies, this bonding scheme usually leads to UV band gaps that limit the overall solar conversion efficiency.

While small polaron formation dynamics are well studied in α-Fe_2O_3, the effect of polaron delocalization on carrier mobilities is not fully understood. In α-Fe_2O_3, the photoexcited electron distorts the local lattice upon the first electron-optical phonon

scattering, forming small polarons that trap photoexcited carriers with a large carrier effective mass. The ~100 fs small polaron formation process can be considered adiabatic, as the on-site reorganization energy is large enough that the small polaron can form without significant carrier thermalization, and it remains trapped until carrier recombination. One proposed approach to suppress small polaron formation is to introduce heteroatoms at a unit cell level to decrease the reorganization energy of the small polaron to less than the thermal energy by expanding its localization radius.[9] This approach has been studied widely in high-throughput synthesis but has yielded mixed performance, partly due to a lack of inclusion of polaron-based physics in the search criteria.[10] The effect of atomic substitutions on small polaron formation dynamics and the correlation to photoexcited charge transport is necessary for improving photocatalysis and engineering other small polaron based applications.

In this work, we measure small polaron formation in $CuFeO_2$ using transient extreme ultraviolet (XUV) spectroscopy. $CuFeO_2$ has a delafossite structure (Figure 4.1(a)) with 2D Cu atomic layers substituted between Fe-O networks, and was identified by high-throughput screening techniques as a potential top performing photocatalyst.[11–13] The Cu atoms affect small polaron formation in two ways, (1) by providing electronic screening between photoexcited polarons in the Fe-O layers, and (2) by allowing the lattice to expand parallel to the Fe-O plane to reduce reorganization potentials. Transient XUV measurements indicate that electronic screening between layers does not change the adiabatic small polaron formation rate from the standard <100 fs measured for almost all Fe(III) compounds to date.[14–16] The ability for the lattice to expand perpendicular to the Fe-O plane, however, is measured to enable a polaron delocalization on a picosecond timescale through a coherent acoustic Cu-(Fe-O) c-axis phonon mode. A corresponding nearest-neighbor Fe(III) to Fe(IV) charge compensation supports the hypothesis of an initial small electron polaron dynamically delocalizing beyond the initial Fe(III) site to the nearest neighbors. This delocalized polaron in turn leads to increased thermally activated hopping relative to the carrier recombination timescale.[15] Beyond photocatalysis, the results provide insight into a broad range of small polaron based materials, and how lattice interactions versus electron correlations can be leveraged to tune their properties.

4.3   Results

Figure 4.1(a) shows the crystal structure of $CuFeO_2$, where the Fe and O sublattices are capped by Cu layers along the c-axis. In the Fe-O sublattice, the Fe atom is
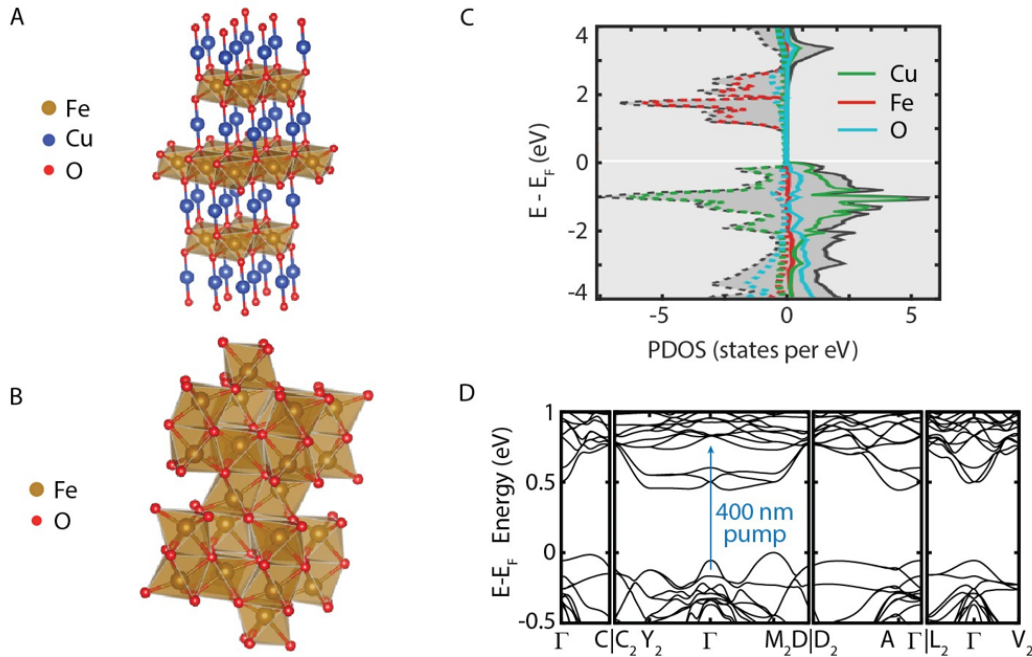
Figure 4.1: A comparison of the (a) delafossite crystal structure of $CuFeO_2$ where Cu atoms are inserted between Fe-O layers and (b) hematite (α-Fe_2O_3). (c) The projected density of states shows that the conduction band is dominated by Fe orbital character while the valence band is mixed Cu-O orbitals.[17] (d) The band structure of $CuFeO_2$, where the 400 nm visible pump is shown to demonstrate the promotion of electrons from the valence band into the conduction band following photoexcitation.

surrounded by oxygen octahedra. This configuration is locally similar to hematite (α-Fe_2O_3), as shown in Figure 4.1(b). α-Fe_2O_3 is a prototypical example of photoexcited small polaron formation at an Fe(III) site and is used as a comparison throughout the paper.[8, 15] Both $CuFeO_2$ and α-Fe_2O_3 are charge-transfer insulators (Figure 4.1(c)). The additional electron density offered by the Cu heteroatoms in $CuFeO_2$ provides hybridization between the Cu and O atoms, which reduces the material's band gap compared to α-Fe_2O_3 and adds dispersion (curvature) to the band structure in the valence band. The conduction band is still relatively flat despite the delocalization offered by the Cu atoms, suggesting that local electron correlations still remain present despite the addition of Cu.

Transient XUV spectroscopy measures small polaron formation dynamics in thin film $CuFeO_2$ following a 3.1 eV (400 nm) photoexcitation of the ligand-to-metal charge-transfer transition from the O 2p orbital to the Fe 3d orbital. The XUV pulse is generated from few-cycle broadband white light with energy centered around the

Fe $M_{2,3}$ edge. Transient XUV reflection spectroscopy is performed at a 10° grazing incidence angle, resulting in a penetration depth estimated as ~2 nm from extinction coefficients. After photoexcitation, the change in the XUV spectrum is defined as $\Delta OD = -\log_{10}(I_{\text{pump on}}/I_{\text{pump off}})$. Under this convention, the increase in spectral intensity (red color) is roughly associated with increased absorption whereas the blue color is roughly associated with decreased absorption. More accurately, the underlying differences between real and imaginary changes in the refractive index versus transmission measurements are important for comparison to theory.
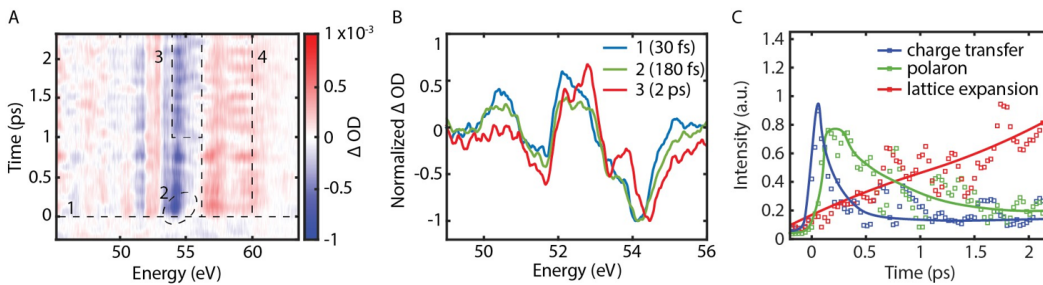

Figure 4.2: (a) Transient XUV reflection-absorption spectra of $CuFeO_2$ following photoexcitation with a 400 nm pump. The red and blue colors represent increased and decreased absorption after photoexcitation, respectively. Four main spectral features are labeled in the plot. At pump-probe overlap (t_0), a series of positive and negative peaks are observed (label 1). Immediately after photoexcitation, an ultrafast spectral blue shift is observed around 55 eV (label 2), which is attributed to octahedra expansion and small polaron formation. At longer pump-probe time delays, spectral intensity and energy oscillations are observed (label 3), which is attributed to polaron induced coherent acoustic phonons. At higher XUV transition energies, increased XUV absorption is observed and attributed to photoinduced Fe^{4+} states (label 4). Experimental lineouts (b) at 30 fs (blue), 180 fs (red), and 2.04 ps (green) which correspond to dynamics in label 1, label 2, and label 3, respectively. The blue trace best represents the charge-transfer state, while the red trace represents the polaronic state, and the final state with the lattice expanded is represented by the green trace. Kinetics plot (c) of the charge transfer (blue), polaron (green), and lattice expansion (red) states with "best fit" lines to visualize the kinetics chosen dynamics while disregarding the coherent phonon oscillations.

The measured transient XUV spectra for the Fe $M_{2,3}$ edge is shown in Figure 4.2. Four distinct spectral features are identified (Figure 4.2(a)). Immediately following photoexcitation, a series of positive and negative spectral features occur between 51 and 56 eV (Figure 4.2(a), label 1). This initial spectrum is followed by a fast spectral blue shift around 55 eV within the first ~300 fs (Fig. 4.2(a), label 2). There are both intensity and energy oscillations in the measured spectra at longer time delays.

A clear intensity oscillation is observed for the main negative peak at 55 eV. An increased oscillation in spectral density occurs between 55.5 eV and 56.6 eV, which is out-of-phase compared to the oscillation of the main negative peak between the 54.5 eV and 55.5 eV (Fig. 4.2(a), label 3). In addition to the features between 51 eV and 56 eV, there are two major absorption peaks above 56 eV. These peaks emerge immediately after photoexcitation, and exhibit oscillating spectral features that strongly correlate with spectral intensities below 56 eV and are in-phase with the oscillations between 54.5 eV and 55.5 eV. While the features in labels 1 and 2 are common among transient XUV measurements of α-Fe_2O_3 and other Fe(III) small polaron materials, the features in labels 3 and 4 are not typically observed in the transient XUV spectra of photoexcited iron oxides. This difference in spectral features suggests that the Cu interstitial layer between the Fe-O octahedra influences later timescale dynamics.

The observed spectral changes are rooted in changes to the screening and angular momentum coupling X-ray transition Hamiltonian. For the Fe $M_{2,3}$ edge, the X-ray transition Hamiltonian is dominated by angular momentum coupling, so the changes in the measured spectra relate more to oxidation states and local bonding effects as compared to state-filling of photoexcited carriers.[18] To understand the spectral features, we simulate the transient XUV reflection spectra of $CuFeO_2$ using a previously reported adiabatic approximation to an ab initio excited state Bethe-Salpeter equation (BSE) treatment of the XUV spectra.[18, 19] Figure 4.3(a) compares experimental spectral lineouts taken from 30 fs after photoexcitation and 2 ps after photoexcitation (Figure 4.3(a)) with BSE theory. The lineout at earlier times corresponds to an initial photoexcited charge-transfer state while the later time lineout shows the polaron state, matching previously measured Fe(III) polaron dynamics.[15, 16] The experimental lineouts follow the theoretically predicted changes in terms of the shift of the zero-crossing and the appearance of a new multiplet-peak at 54.5 eV.

The spectral features in labels 3 and 4 indicate the dynamics of $CuFeO_2$ that differ from previously measured iron oxide materials. The spectral splitting seen in Figure 4.2(a), label 3 matches theory for an overall isotropic lattice expansion in the unit cell starting around one picosecond after the small polaron has formed. When the small polaron is formed, the oxygen octahedra around the new Fe^{2+}-like site expand locally due to the reduced Coulomb attraction between Fe and O atoms. The secondary, local lattice expansion around the polaron site reduces the

bond length between the oxygen and nearest neighboring Fe sites through a c-axis expansion, delocalizing the polaron wavefunction from its initial state. The lattice expansion correlates with coherent phonon oscillations measured within this region. Specifically, intensity modulation occurs between 55.4 eV and 56.4 eV that oscillates out-of-phase compared to the intensity between 54.5 eV and 55.2 eV (Fig. 4.2(a), labels 3 and 4). The differential spectra between 55.4–56.4 eV is plotted in Figure 4.3(c). Initial features are damped due to the optical phonons associated with small polaron formation. After ~1 ps, a Fourier analysis reveals that dominant oscillations at 1 and 5.3 THz are present (Fig. 4.3(d)). These frequencies correspond to acoustic Cu-(Fe-O) modes along the c-axis and a mixture of acoustic and optical phonons of the Fe-O bond, respectively, confirming the coupling between the polaron-induced octahedra expansion and the lattice expansion along the c-axis between Cu and Fe-O planes.[20]

The spectral features above 56 eV (Fig. 4.2(a), label 4) are well represented by the formation of a local Fe(IV) state immediately after photoexcitation, which would agree with a delocalization of the Fe(II) small polaron state through lattice expansion. This feature also possesses oscillations that are in-phase with the Fe-O and Cu-O bond motions seen in the negative spectral features at 1 and 5.3 THz and plotted in Figure 4.3(c and d). While a pure oxidation state is challenging to model using the DFT-BSE calculations (given that carrier states are filled up to the photoexcited energy in the adiabatic perturbation limit), a ligand field theory calculation reinforces that the increased XUV absorption above 56 eV is due to Fe^{4+} absorption (Fig. 4.3(b)).[21] The only possible oxidation state in $CuFeO_2$ in the ground state is Fe^{3+}. Our measurement suggests that there is a sudden increase in Fe^{4+} states immediately after photoexcitation and the charge-transfer transition. This state then oscillates in-phase with the Fe-O and Cu c-axis lattice motions.

The kinetics for each spectral feature are shown in Figure 4.2(c). The Fe(IV) state in the nearest-neighbor shell forms during the the Fe(III) to Fe(II) charge transfer transition (Fig. 4.2(c) blue trace) immediately after photoexcitation. However, the polaron delocalization signal does not appear until the ~1 ps timescale, compared to the ~100 fs small polaron formation time constant reported here (Fig 4.2(c) green trace) and in other Fe(III) oxide systems.[15, 16] The transient XUV data confirms that the Cu-hybridization does not change the small polaron formation energy or kinetics through electronic screening, but rather reduces the on-site reorganization energy that ultimately delocalizes the small polaron. The small polaron formation
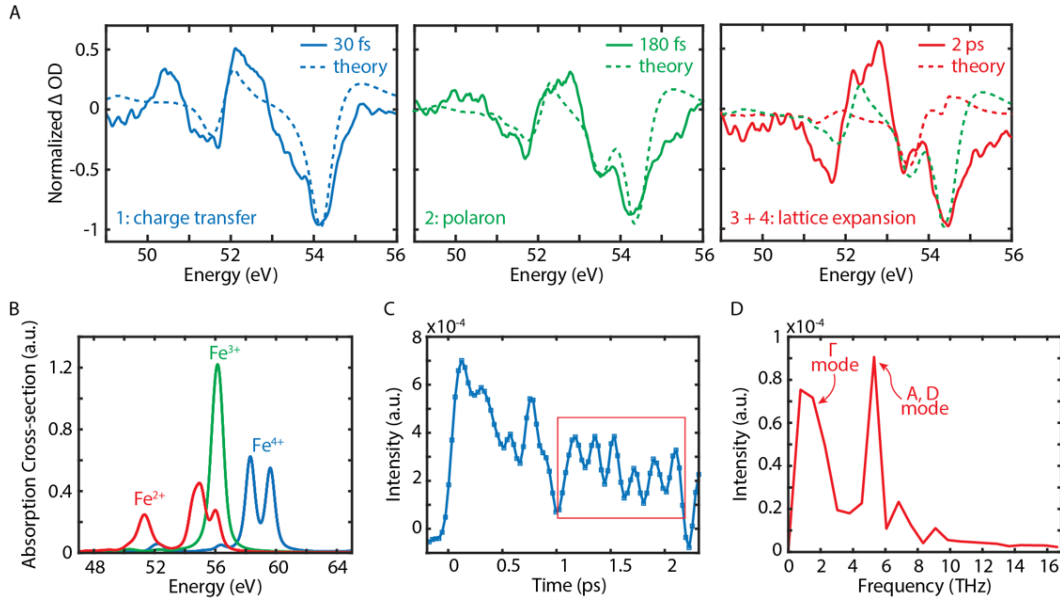
Figure 4.3: Comparison of experiment and theory. Experimental lineouts (solid lines) (a) compared to BSE theory (dashed lines) for immediately after photoexcitation (blue), following polaron formation (green), and the change to the polaron spectrum following lattice expansion (red), which correspond the label 1, label 2, and labels 3 and 4 in Figure 4.2(a), respectively. Ligand-field theory (b) for differing oxidation states of iron. The blue trace corresponding to Fe^{4+} appears at the same energy as Figure 4.2(a), label 4. The spectral oscillations (c) in the main negative feature at ~55 eV in Figure 4.2(a) label 3. The oscillations in the red box were Fourier transformed (d) and demonstrate Cu c-axis acoustic mode at 1 THz and a mixture of Fe-O modes at 5.3 THz.

and delocalization process is shown schematically in Figure 4.4 for both α-Fe_2O_3 and $CuFeO_2$. In α-Fe_2O_3, the charge transfer initiated by photoexcitation induces a small electron polaronic state resulting in distortion of the lattice and trapping of the charge carrier until recombination. In $CuFeO_2$, the charge transfer also induces small polaron formation; however, the nearest neighboring atoms compensate this charge transfer by becoming Fe^{4+} in character. This charge compensation enables a lattice expansion that leads to polaron delocalization on a picosecond timescale.

The outcomes of this work provide new insight into small polaron dominated materials and phenomena. We did not find that the Cu atom hybridization changes the small polaron formation rate, most likely due to strong Fe-Fe electron correlations. Instead, changing the lattice degrees of freedom appears to correlate with increasing the transport of the small polarons by lowering the polaron reorganization energies. Surprisingly, delocalization is a dynamical process following adiabatic small po-
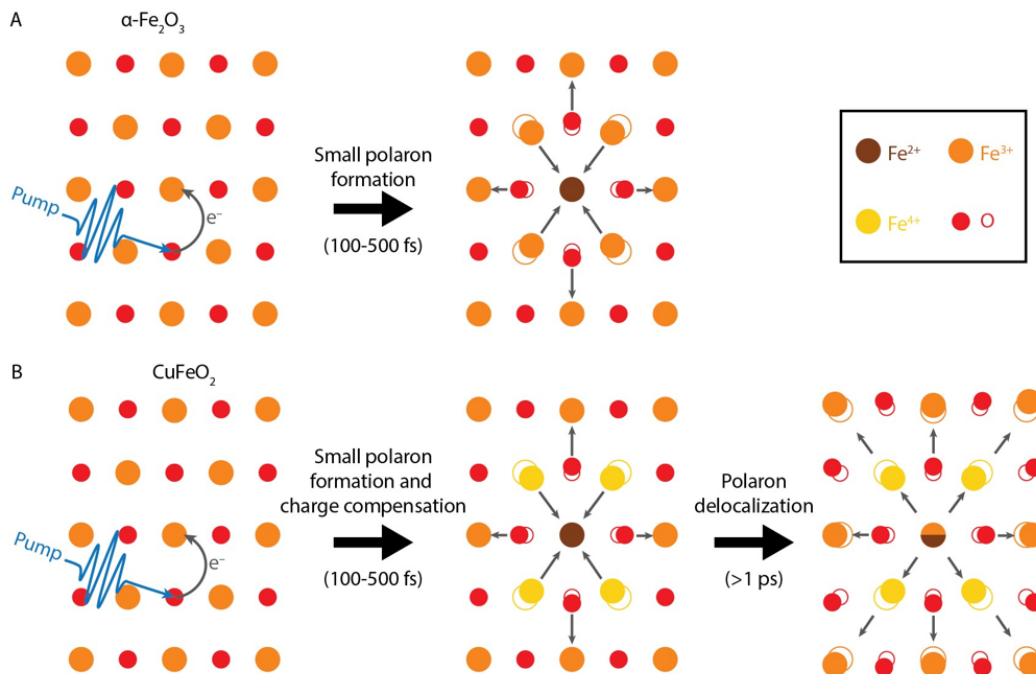
Figure 4.4: Schematic representation of polaron formation mechanisms in (a) α-Fe_2O_3 and (b) $CuFeO_2$. In $CuFeO_2$ the formation of Fe^{4+} states around polaron sites and the isotropic expansion of the lattice enables delocalization of the polarons on a ps timescale.

laron formation, going against the step-wise framework of carrier thermalization and delocalized polaron formation occuring sequentially. These insights are useful for both the materials-engineering of larger radius and more mobile polarons in transition metal oxides, as well as the coherent control of the lattice response to small polaron formation.

References

(1) Mott, N. F. Polaron Models of High-Temperature Superconductors. *Journal of Physics: Condensed Matter* **1993**, *5*, 3487–3506, DOI: 10.1088/0953-8984/5/22/003.

(2) Zhang, C.; Sous, J.; Reichman, D. R.; Berciu, M.; Millis, A. J.; Prokof'ev, N. V.; Svistunov, B. V. Bipolaronic High-Temperature Superconductivity. *Physical Review X* **2023**, *13*, 011010, DOI: 10.1103/PhysRevX.13.011010.

(3) Kudinov, E. K. Model of a Polaron Superconductor. *Physics of the Solid State* **2002**, *44*, 692–703, DOI: 10.1134/1.1470561.

(4) Nosarzewski, B.; Huang, E. W.; Dee, P. M.; Esterlis, I.; Moritz, B.; Kivelson, S. A.; Johnston, S.; Devereaux, T. P. Superconductivity, Charge Density Waves, and Bipolarons in the Holstein Model. *Physical Review B* **2021**, *103*, 235156, DOI: `10.1103/PhysRevB.103.235156`.

(5) Ghosh, R.; Spano, F. C. Excitons and Polarons in Organic Materials. *Accounts of Chemical Research* **2020**, *53*, 2201–2211, DOI: `10.1021/acs.accounts.0c00349`.

(6) Zhang, L.; Chu, W.; Zhao, C.; Zheng, Q.; Prezhdo, O. V.; Zhao, J. Dynamics of Photoexcited Small Polarons in Transition-Metal Oxides. *The Journal of Physical Chemistry Letters* **2021**, *12*, 2191–2198, DOI: `10.1021/acs.jpclett.1c00003`.

(7) Yim, C. M.; Watkins, M. B.; Wolf, M. J.; Pang, C. L.; Hermansson, K.; Thornton, G. Engineering Polarons at a Metal Oxide Surface. *Physical Review Letters* **2016**, *117*, 116402, DOI: `10.1103/PhysRevLett.117.116402`.

(8) Biswas, S.; Wallentine, S.; Bandaranayake, S.; Baker, L. R. Controlling Polaron Formation at Hematite Surfaces by Molecular Functionalization Probed by XUV Reflection-Absorption Spectroscopy. *The Journal of Chemical Physics* **2019**, *151*, 104701, DOI: `10.1063/1.5115163`.

(9) Gregoire, J. M.; Zhou, L.; Haber, J. A. Combinatorial Synthesis for AI-driven Materials Discovery. *Nature Synthesis* **2023**, *2*, 493–504, DOI: `10.1038/s44160-023-00251-4`.

(10) Nguyen, T. H.; Zhang, M.; Septina, W.; Ahmed, M. G.; Tay, Y. F.; Abdi, F. F.; Wong, L. H. High Throughput Discovery of Effective Metal Doping in $FeVO_4$ for Photoelectrochemical Water Splitting. *Solar RRL* **2020**, *4*, 2000437, DOI: `10.1002/solr.202000437`.

(11) Zhao, T.; Liu, Q.-L.; Zhao, Z.-Y. High-Throughput Screening Delafossite $CuMO_2$ (M = IIIA, 3d, 4d, 5d, and RE) Optoelectronic Functional Materials Based on First-Principles Calculations. *The Journal of Physical Chemistry C* **2019**, *123*, 14292–14302, DOI: `10.1021/acs.jpcc.9b04481`.

(12) Saadi, S.; Bouguelia, A.; Trari, M. Photocatalytic Hydrogen Evolution over $CuCrO_2$. *Solar Energy* **2006**, *80*, 272–280, DOI: `10.1016/j.solener.2005.02.018`.

(13) Wolf, M.; Madsen, G. K. H.; Dimopoulos, T. Accelerated Screening of Cu–Ga–Fe Oxide Semiconductors by Combinatorial Spray Deposition and High-Throughput Analysis. *Materials Advances* **2023**, *4*, 2612–2624, DOI: `10.1039/D3MA00136A`.

(14) Carneiro, L. M.; Cushing, S. K.; Liu, C.; Su, Y.; Yang, P.; Alivisatos, A. P.; Leone, S. R. Excitation-Wavelength-Dependent Small Polaron Trapping of Photoexcited Carriers in α-Fe_2O_3. *Nature Materials* **2017**, *16*, 819–825, DOI: `10.1038/nmat4936`.

(15) Husek, J.; Cirri, A.; Biswas, S.; Baker, L. R. Surface Electron Dynamics in Hematite (-Fe_2O_3): Correlation between Ultrafast Surface Electron Trapping and Small Polaron Formation. *Chemical Science* **2017**, *8*, 8170–8178, DOI: `10.1039/C7SC02826A`.

(16) Vura-Weis, J.; Jiang, C.-M.; Liu, C.; Gao, H.; Lucas, J. M.; de Groot, F. M. F.; Yang, P.; Alivisatos, A. P.; Leone, S. R. Femtosecond $M_{2,3}$-Edge Spectroscopy of Transition-Metal Oxides: Photoinduced Oxidation State Change in -Fe_2O_3. *The Journal of Physical Chemistry Letters* **2013**, *4*, 3667–3671, DOI: `10.1021/jz401997d`.

(17) Jain, A.; Ong, S. P.; Hautier, G.; Chen, W.; Richards, W. D.; Dacek, S.; Cholia, S.; Gunter, D.; Skinner, D.; Ceder, G.; Persson, K. A. Commentary: The Materials Project: A Materials Genome Approach to Accelerating Materials Innovation. *APL Materials* **2013**, *1*, 011002, DOI: `10.1063/1.4812323`.

(18) Klein, I. M.; Liu, H.; Nimlos, D.; Krotz, A.; Cushing, S. K. *Ab Initio* Prediction of Excited-State and Polaron Effects in Transient XUV Measurements of α-Fe_2O_3. *Journal of the American Chemical Society* **2022**, *144*, 12834–12841, DOI: `10.1021/jacs.2c03994`.

(19) Liu, H.; Michelsen, J. M.; Mendes, J. L.; Klein, I. M.; Bauers, S. R.; Evans, J. M.; Zakutayev, A.; Cushing, S. K. Measuring Photoexcited Electron and Hole Dynamics in ZnTe and Modeling Excited State Core-Valence Effects in Transient Extreme Ultraviolet Reflection Spectroscopy. *The Journal of Physical Chemistry Letters* **2023**, *14*, 2106–2111, DOI: `10.1021/acs.jpclett.2c03894`.

(20) Klobes, B.; Herlitschke, M.; Rushchanskii, K. Z.; Wille, H.-C.; Lummen, T. T. A.; Van Loosdrecht, P. H. M.; Nugroho, A. A.; Hermann, R. P. Anisotropic Lattice Dynamics and Intermediate-Phase Magnetism in Delafossite $CuFeO_2$. *Physical Review B* **2015**, *92*, 014304, DOI: `10.1103/PhysRevB.92.014304`.

(21) Stavitski, E.; De Groot, F. M. The CTM4XAS Program for EELS and XAS Spectral Shape Analysis of Transition Metal L Edges. *Micron* **2010**, *41*, 687–694, DOI: `10.1016/j.micron.2010.06.005`.

Appendix A

SUPPLEMENTARY INFORMATION: MEASURING PHOTOEXCITED ELECTRON AND HOLE DYNAMICS IN ZNTE AND MODELING EXCITED STATE CORE-VALENCE EFFECTS IN TRANSIENT EXTREME ULTRAVIOLET REFLECTION SPECTROSCOPY

This appendix contains supplementary information for Chapter 3. The content is adapted with permission from:

A.1 Dopant characterization of intrinsic bulk ZnTe

To rule out the possibility of mid-gap defect states that could potentially lead to the experimentally observed transient decrease in reflectivity within the gap, we perform X-ray photoemission spectroscopy (XPS) and a 4-point probe measurement on intrinsic bulk ZnTe.
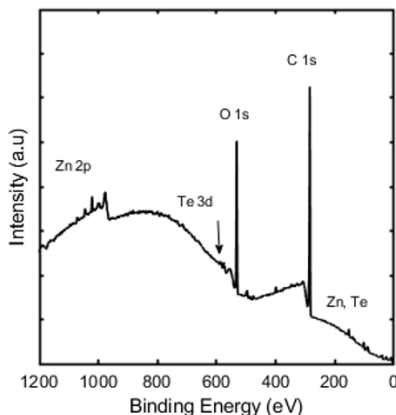
Figure A.1: XPS measurements on intrinsic bulk ZnTe. Carbon and oxygen are observed on the surface. No heteroatom dopants are observed.

Figure A.1 shows an XPS survey on bulk ZnTe. While carbon and oxygen on the surface are observed, there is no evidence for hetero-atom dopants. Quantification furthers shows a roughly 50:50 Zn:Te ratio. Figure A.2 shows the 4-point probe measurements. The resistivity is measured to be $\rho=(1.26\pm0.3)\times10^9$ $\Omega\cdot$cm. The dopant density n is related to the resistivity via $\rho = \frac{1}{e\mu n}$, where μ is carrier mobility and is estimated to be $\mu \approx 100$ cm$^2\cdot$V$^{-1}\cdot$ s^{-1}. The dopant density is estimated at 5×10^7 cm^{-3}. The dopant density is too small to be responsible for the observed mid-gap transient spectral feature, whose amplitude is comparable to the transient reflectivity change caused by high concentrations of photoexcited carriers at 10^{20} cm^{-3}.
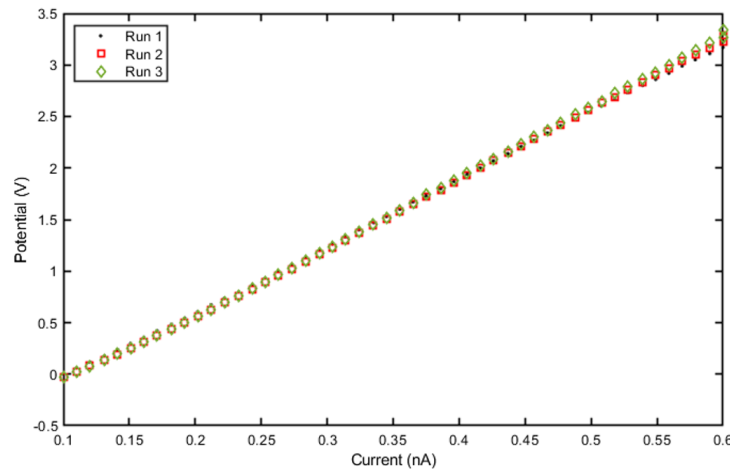

Figure A.2: 4-point probe measurements of resistivity and dopant density on intrinsic bulk ZnTe.

A.2 Growth and structural characterization of sputter-deposited ZnTe thin films

ZnTe thin films were prepared on a 50.8 mm x 50.8 mm Corning EXG glass substrate by RF sputtering from a ZnTe target. A stainless-steel 130 m thick shadow mask was placed over the substrate to create two distinct regions: a large blanket film and smaller discrete patterns. The substrate + mask assembly was clamped to an Inconel plate which was heated by a SiC serpentine resistance heater. The plate was held at the setpoint of 300 °C for a minimum of 1 hour prior to deposition. Chamber pressure at this temperature was 3 x 10^{-7} Torr prior to flowing any process gases. During the sputter process, 16 sccm of Ar was flowed through the system and the pumping was throttled to achieve the desired growth process pressure of 2.7 mTorr. The plate was rotated at approximately 30 revolutions per minute

during the 2-hour growth. Samples were cooled under Ar prior to being removed from the growth chamber. The blanket region of the ZnTe film was characterized by X-ray diffraction (XRD) at 22 distinct points (Figure A.3) to verify structural uniformity as a function of position. XRD patterns were collected by a 2D solid state detector scanning in an ω-2θ geometry using Cu-Kα radiation. Figure A.4 shows the resulting XRD patterns for all 22 points as a false color plot. No appreciable changes were observed in diffraction patterns between points. An intensity vs. 2θ line scan from point 10 is also shown. Comparing the experimentally measured diffraction pattern against a simulated pattern generated using a reference ZnTe crystallographic information file (Inorganic Crystal Structure Database entry 77072), we find that the peak positions match and the ZnTe film adopts the expected zincblende crystal structure. The high relative intensity of the (111) peak at ca. 25° in the experimental data (versus the reference pattern) is attributed to crystallographic texture. Figure A.5 shows film thickness measurements collected from three different regions using a stylus profilometer. The regions were from the masked portions of the film and geometrically equivalent to the positions of points 3, 9, and 17 (Figure A.3). Raw profilometry data were notably sloped and bowed. A first-order polynomial subtraction was carried out to flatten the profiles over the region of interest (i.e., the masked ZnTe sample), but higher-order bowing was ignored. As seen in Figure A.3, the sampled points are ca. 400-450 nm thick. It is difficult to pinpoint whether any discrepancies between the points are due to non-uniformity or experimental factors, such as substrate topology, shadowing from the stainless-steel mask. 100 nm thick calibration samples grown with nominally identical chamber conditions were measured by X-ray reflectometry (XRR), and thicknesses over a similar area were uniform to ±2 nm with <1 nm RMS roughness.

A.3   Ground state optical sample characterization

The band gap of both bulk and thin film ZnTe was determined using UV-VIS spectroscopy (Cary 5000) (Figure A.6, A.7). The PRISA software was used to calculate the bandgap of the thin film sample while also mitigating thin-film interference effects.[1] Figures A.6 and A.7 present $(\alpha hv)^{1/r}$ vs energy plots where r = 1/2 for direct allowed transitions. The estimated direct bandgap is found to be 2.19 eV and 2.18 eV for bulk and thin films, respectively.
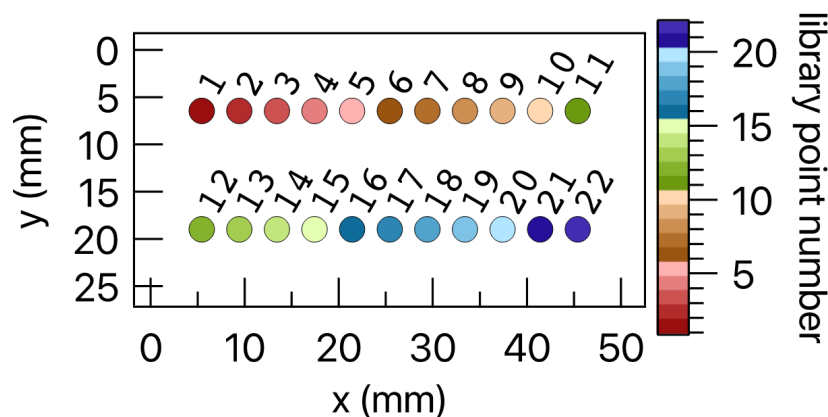
Figure A.3: Spatial map of point locations on a 25.4 mm by 50.8 mm region of the glass substrate used to verify uniformity of ZnTe thin films.
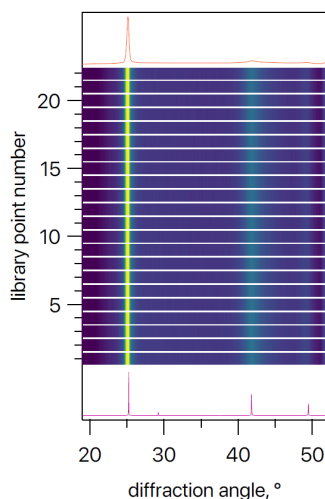

Figure A.4: X-ray diffraction from the ZnTe thin films. The false color map shows uniformity of the XRD patterns from the 22 sampled points. A reference pattern (generated from Inorganic Crystal Structure Database entry 77072) and line scan (collected from point 10) presented using more typical intensity vs. 2θ axes are also provided.

A.4 Experimental setup: Transient extreme ultraviolet reflection spectrometer

The reported bulk ZnTe measurements are obtained using photoexcitation of a ~50 fs, 400 nm frequency doubled output of a BBO crystal with p-polarization, pumped with an 800 nm, 1 kHz regeneratively amplified Ti:Sapphire laser (Coherent Legend Elite Duo). The optical excitation fluence is 1.74 mJ/cm^2, resulting in an initial photoexcited carrier density of 5.41×10^{20} cm^{-3}. Transient reflection is measured by
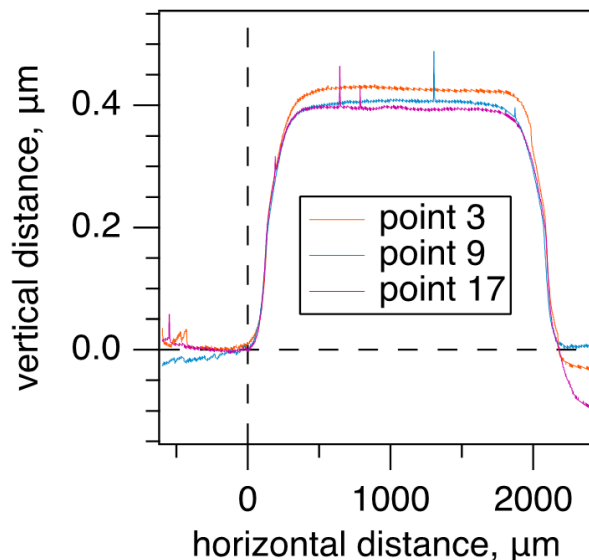
Figure A.5: Stylus profilometry collected from ZnTe thin films. Data were collected from a part of the substrate with masked regions, with the points being symmetrically equivalent during growth to those shown in Figure A.3.
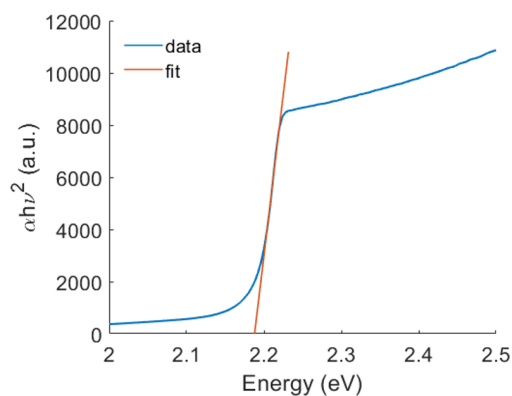

Figure A.6: Tauc plot of the ZnTe bulk. The direct band gap is measured to be 2.19 eV.

varying delay times between the excitation and probe pulses using an optomechanical delay stage. The photoexcited carrier dynamics are probed with an XUV pulse produced by high-harmonic generation in argon with an s-polarized few-cycle white light pulse (<6 fs, 550 nm - 950 nm, Figure A.8). The residual white light beam is removed with a 200 nm thick Al filter (Lebow). The generated XUV continuum is used to probe the Te $N_{4,5}$ absorption edges around 40 eV. A typical XUV spectrum is shown in Figure A.9. An edge-pixel referencing scheme was used to reduce noise due to intensity fluctuations based on signal-free spectral regions.[2] The reflection
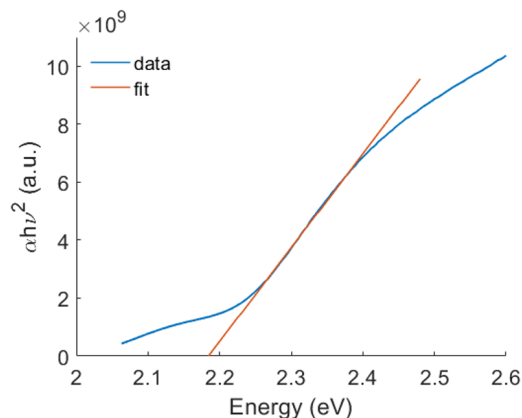
Figure A.7: Tauc plot of ZnTe thin film. The direct band gap is measured to be 2.18 eV.

measurement uses a 10-degree grazing incidence geometry (80 degrees from normal incidence). The static sample reflectivity around the Te $N_{4,5}$ edge is shown in Figure A.10. The reflectivity decreases around the conduction band minimum (around 40 eV from Te 4d core states). The static XUV reflectivity of ZnTe is found by dividing the measured static reflectivity spectrum of ZnTe by the static reflectivity of a Si wafer, which does not have any absorption features in this energy region.

A.4.1 Characterization of few-cycle white light pulse for XUV pulse generation

A dispersion scan (d-scan, Sphere Ultrafast Photonics)[3] was used to characterize the broadband white light few-cycle pulse used for XUV pulse generation. In this method, a pair of glass wedges with known dispersion are inserted in the beam path. The second harmonic spectra of the white light generated with a BBO crystal are measured as a function of introduced dispersion through wedge insertion. The electric field of the few-cycle pulse can be retrieved based on the reconstruction algorithm of the d-scan trace.

A.4.2 Representative XUV probe spectrum

The XUV probe pulse is produced through high-harmonic generation in an Ar gas cell. Figure A.9 shows a representative normalized XUV spectrum reflected from ZnTe with a 10 degree incident angle (80 degrees from normal incidence).
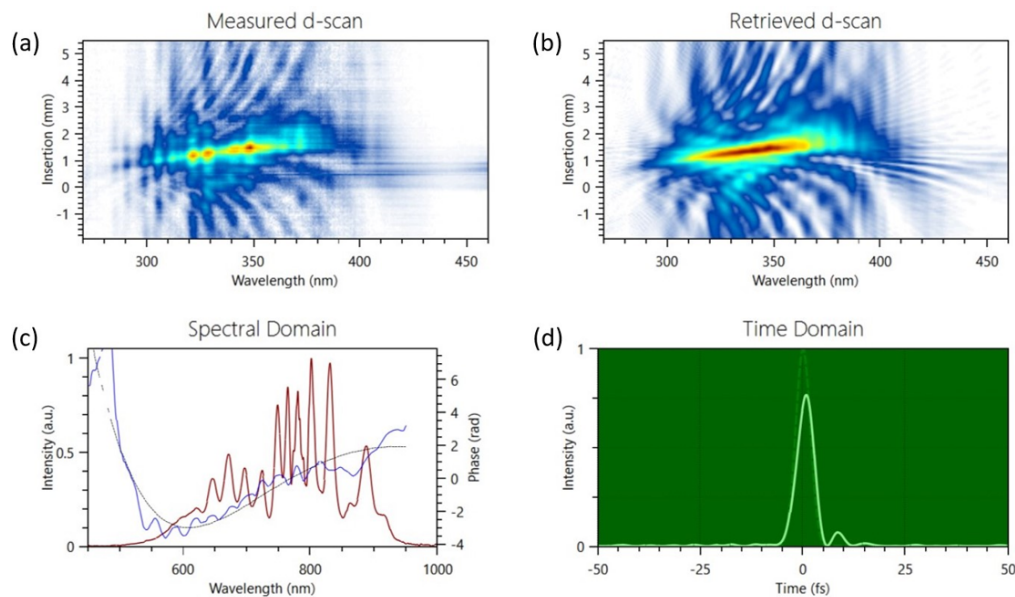
Figure A.8: Characterization of few-cycle white light pulse with dispersion scan (d-scan). (a) Measured second harmonic spectra as a function of wedge insertion. (b) Reconstructed d-scan trace. (c) White light spectrum (red line), spectral phase (blue line) and polynomial fit of the spectral phase (black line). (d) Retrieved white light pulse has an intensity profile with a temporal FWHM of 4.9 fs.

A.5 Theoretical methods: Ground state and excited state core-level spectra

To fully analyze the transient core-level spectra, state blocking, and the associated changes in screening of the core-valence exciton must be considered, as well as any potential change in spin-orbit coupling and angular momentum effects. These changes are calculated using an ab initio combined theoretical approach based on density functional theory (DFT) and the Bethe-Salpeter equation (BSE). The existing OCEAN code (Obtaining Core-level Excitations using Ab initio calculations and the NIST BSE solver)[4, 5] is modified to accept excited state distributions to determine how the ground state band structure relates to the observed XUV spectra and transient changes. In this procedure, the band structure and the ground state wavefunction are first calculated using DFT (Quantum Espresso)[6]. The BSE is solved to obtain core-valence exciton wavefunctions including spin-orbit coupling and Coulomb screening of the core-valence exciton. The reflectivity spectra are calculated from the complex dielectric function as calculated by OCEAN and converted using the Fresnel equations.
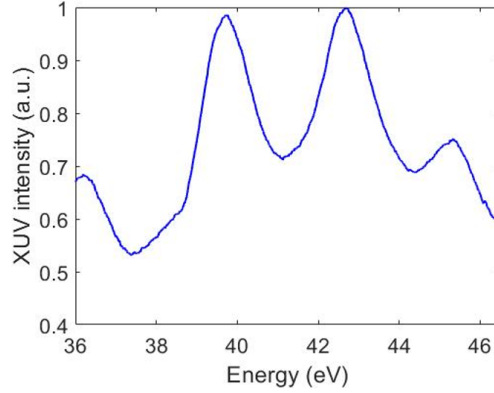
Figure A.9: Representative reflected XUV spectrum from ZnTe with a 10 degree incident angle relative to the sample surface (80 degrees from normal incidence). The energy range of the selected spectrum is defined by the physical size and position of the detector to cover the Te $N_{4,5}$ edge.

A.5.1 Ground state calculation

XUV reflection spectra were calculated with the OCEAN[4, 5] code based on a converged DFT calculation[6]. The DFT and BSE calculations are solved using a 20 × 20 × 20 k-point mesh. We use 9 valence bands and 31 conduction bands in our calculation. The DFT calculation uses the norm-conserving generalized gradient approximation (GGA), Perdew-Burke-Enzerhof (PBE) pseudopotentials, a 300 Rydberg energy cut-off, and a converged lattice constant of 6.10 Å. The OCEAN code uses the projector augmented wave method (PAW) to calculate core-level transition matrix elements, which are then used in the BSE equation to calculate final states as modified by the core hole. The OCEAN BSE calculation uses a screening mesh of 4 × 4 × 4, a dielectric constant of 10.4, a 4.0 Bohr screening radius, and a 0.7 scaling factor for the slater G parameter. A post-calculation broadening is used as a fitting method to achieve similar linewidth to that observed in the experiment. The DFT calculation underestimates the band gap of ZnTe. After DFT calculation, we add a band gap correction by scissor shifting conduction bands up by 1.02 eV to achieve a correct band gap. In this theoretical framework, both the real and imaginary dielectric function are directly calculated in the OCEAN code, allowing easy comparison between theory and experiments done in transmission or reflection configurations.

Figure A.10 shows the calculation of the ground state complex dielectric function (Figure A.10(a)), as well as the calculated reflectivity, overlaid with the experimentally measured static sample reflection around the Te $N_{4,5}$ edge (Figure A.10(b)).
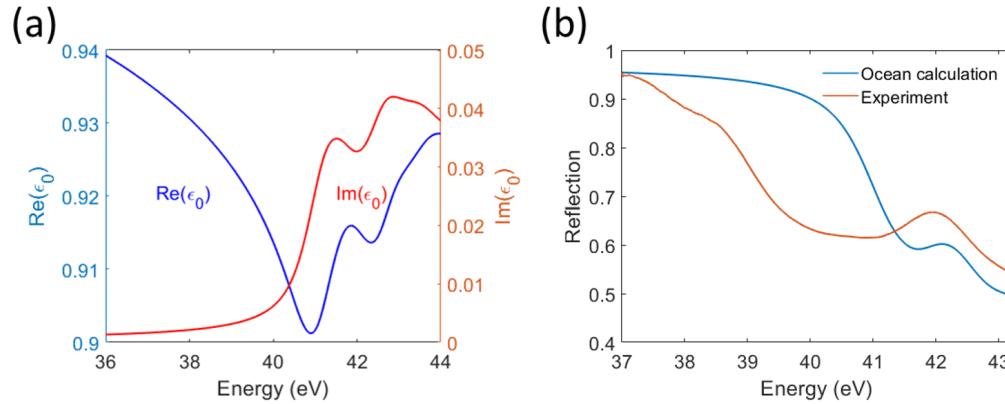
Figure A.10: (a) Calculated ground state complex dielectric constant. (b) Calculated ground state reflectivity, overlaid with experiment. Experimentally measured refection is normalized to a Si wafer to remove the high harmonic profile in the spectra.

The measured ZnTe XUV reflection is normalized to a Si wafer, which doesn't exhibit any sharp spectral features around 40 eV. By referencing to Si, the typical high-harmonic intensity profile is removed from the static reflection spectrum. However, the absolute reflectivity of ZnTe and Si is difficult to obtain as variance of sample surface roughness affects XUV reflectivity, such as Debye-Waller factors. For this reason, a normalized reflectivity is shown in Figure A.10(b).

As shown in Figure A.10, the OCEAN calculation reproduces Te edges. However, it underestimates the pre-edge absorption. In OCEAN, the calculation assumes perfect crystals, where there is no pre-edge absorption. For actual samples used in experiments, many effects can contribute to the pre-edge absorption, including but not limited to an imperfect crystal lattice, surface states, an imperfect bonding environment, and surface-modified lattice configurations. We note that the discrepancy between the calculated and measured ground state reflection plays a much lesser role in the excited states interpretation. The reason is that for the excited states calculation, we compare the changes in transient reflectivity, defined as $\Delta OD = -\log_{10} \frac{I_{pump\ on}}{I_{pump\ off}}$. Under this definition, systematic error such as underestimated pre-edge absorption largely cancels during the normalization between pump on and pump off spectra.

A.5.2   Excited state calculation

To capture the photoexcited electrons and holes, we modify the OCEAN package, which allows us to selectively forbid or allow XUV transitions to the conduction or valence bands at different momentum k-points. In this experiment, we aim to understand carrier thermalization from the initial photoexcited states to the band gap minimum at the Γ point. To simulate this charge transfer process, we discretize the states between the initial photoexcited states and the final states across the direct band gap at the Γ point into a combination of 9 different electron configurations in the conduction bands and 9 different hole configurations in the valence band. The discretization is based on the energy difference between conduction and valence bands. As a result, each discretized electron and hole configuration consist of multiple k-points in momentum space. The calculated excited states spectra of the total 81 combined electron and hole configurations is shown in Figure A.11. The calculation is performed on a 20 × 20 × 20 mesh in k-space. Under this condition, both electron and hole thermalization can be seen, with electron and hole energy resolution at ~60 meV (calculated carrier energy difference between neighboring hole configurations). Better resolution can be further achieved by increasing the k-space sampling rate or interpolating the spectra between adjacent carrier distributions.

The momentum-resolved differential XUV transition probability amplitudes in Fig. 3.2(b) are calculated by solving the core-valence wavefunctions using the OCEAN generalized minimal residual method (GMRES) solver instead of the Haydock method used for calculations of spectra.[7]

When comparing theory with experiment, it is worth noting that in the excited states calculation, we do not input the actual carrier density (in units of 10^{20}/cm^3) in our calculation. Rather, we fully allow or forbid XUV transition to certain states in the conduction or valence bands. For this reason, we do not simulate carrier density evolution as a function of time, which is encoded in spectral intensity and is related to recombination and diffusion. It is the simulated peak position, or peak energy (related to the hot carrier energy), rather than peak amplitude (associated with carrier density) that we use to compare between experiment and theory.

A tentative reconstruction of the transient data is shown in Figure 3.2(c) of the main text, where we fit the calculated excited state spectra to the measured transient spectra at each pump-probe time delay. The reconstruction is performed for the first 800 fs after photoexcitation, before phonon modulation dominates the spectra while

the carrier relaxation largely finishes. Initial hot electron and hole thermalization is observed in the theoretical reconstructed transient XUV spectra. While an overall thermalized trend can be reconstructed, in the current example it is difficult to assign the measured transient reflectivity at each pump-probe delay to a unique carrier configuration. The resolution is limited by k-space sampling rate, small excess kinetic energy of carriers from photoexcitation, and spectral fluctuations from the experiment. This method will work best when the hot carriers have large excess kinetic energy compared to the band gap and when the band structure is highly dispersive. In principle, this approach allows the theory to reproduce state filling effects, carrier energy and momentum distributions, and relaxation pathways, which could be of importance in various solar-driven semiconductor processes such as multi-exciton generation.
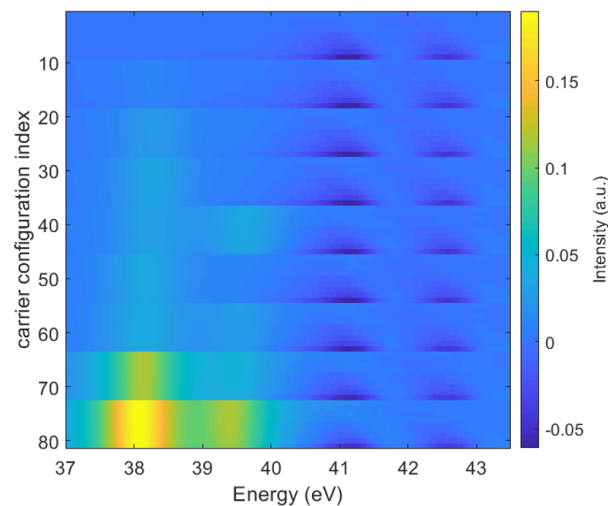

Figure A.11: Calculated excited state XUV differential spectra under different carrier configurations. States between the initial photoexcitation and the final states at the point are discretized into 9 electron energy configurations and 9 holes energy configurations, with a combined total 81 unique electron-hole energy configurations. In this plot, 81 configurations are plotted and sorted by increasing electron and hole energy. For example, the carrier configuration indices (y axis) 1 to 9 corresponds to having holes fixed at the lowest energy states (around the point), while sweeping 9 electron configurations from low energies to high energies. Similarly, the carrier configuration indexes 10 to 18 plot the same 9 electron configurations, but under a different hole configuration with a higher hole energy. Clear electron and hole thermalization can be seen in this plot.
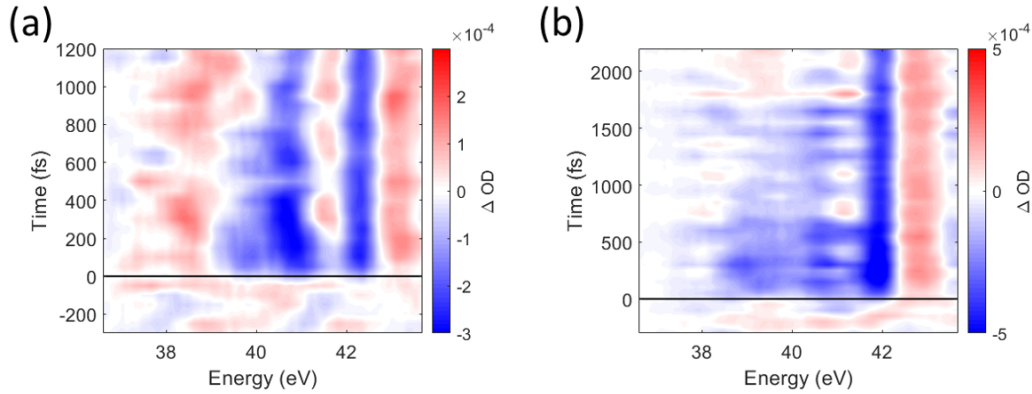
Figure A.12: Transient XUV spectra of ZnTe thin film. (a) Similar transient XUV signature compared to bulk measurements in Figure 3.1 are reproduced on the thin film sample with an excitation density of 1.06 mJ/cm^2, suggesting the mid-gap feature is intrinsic to ZnTe and does not depend on the sample growth method. (b) At a higher excitation intensity of 1.59 mJ/cm^2, both the spectral redshift and the lifetime of the band gap dynamics are increased. This observation is consistent with the assignment of the many-body induced band gap renormalization picture to the measured in-gap dynamics. Spectral intensity oscillations potentially due to acoustic phonons are also observed.

A.6 Transient XUV spectra on ZnTe thin films and under different pump intensities

The many-body nature of the mid-gap transient spectral feature reported in Figure 3.1 is further confirmed by performing a transient XUV reflection measurement on high quality ZnTe thin films (sample characterization in Supplementary Information section A.2). The transient XUV reflection spectra are shown in Figure A.12. In Figure A.12(a), a similar mid-gap transient spectral signature is observed, as compared to the bulk ZnTe measurement reported in the main text. This measurement rules out the possibility of the mid-gap response being dependent on the method of sample growth, and strongly suggests that it is an intrinsic response of ZnTe, regardless of sample growth methods. We further conclude that the mid-gap response depends on the photoexcited carrier density. Figure A.12(b) shows the transient XUV reflection measured at a higher excitation density of 1.59 mJ/cm^2. Under higher carrier density, the mid-gap dynamics are more pronounced, where both the redshift and the lifetime are increased. This is consistent with the assignment of many-body driven band gap renormalization, where higher carrier densities will increase energy shifts as well as increase the lifetime as it takes longer for more carriers to reach equilibrium.
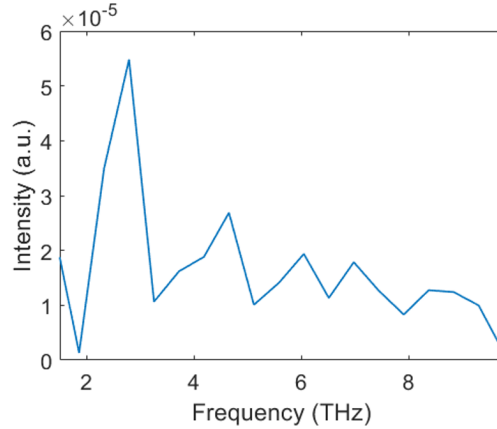
Figure A.13: Fourier analysis of intensity oscillations. Frequency spectrum of intensity oscillations between 40.2 eV and 41.4 eV of the data shown in Figure A.12(b) reveals an oscillation frequency of 2.79 THz. This frequency is associated with acoustic phonon branches with wave vectors between Γ-K and Γ-L regions.

In addition to enhanced band gap dynamics, at higher excitation intensity we also observe strong spectral intensity oscillations (Figure A.12(b)). Fourier transformation between 40.2 eV and 41.4 eV reveals oscillation peaked at 2.79 THz (Figure A.13). This frequency is associated with acoustic phonon branches with wave vectors between Γ-K and Γ-L regions.

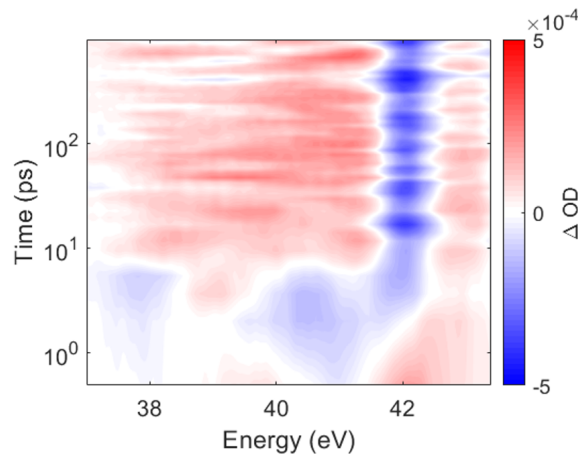## A.7   Nanosecond transient XUV reflection measurement

Figure A.14: Transient XUV reflection measurement up to 1 ns after photoexcitation. No significant carrier recombination is observed, suggesting that the intrinsic carrier lifetime is longer than 1 ns.

As a complementary measurement to the fast femtosecond-to-picosecond carrier

relaxation dynamics presented in the manuscript, here we report the measurement of transient XUV spectra up to 1 ns (Figure A.14). The scanned time points are sampled on a logarithmic scale, and the pump-probe temporal overlap has an offset of 2 ps, as shown in Figure A.14. The spectral intensity of the electronic Te $4d_{5/2}$ to conduction band transition around 40 eV only exists for the first $\sim$10 ps and is quickly replaced with the overlapped Te $4d_{3/2}$ to valence band transition (hole signature). For this reason, we use the intensity of $4d_{3/2}$ to conduction band transition to track the hot carrier lifetime. Unlike the electron and hole diffusion rates of 2.21 ± 1.12 ps and 3.91 ± 3.58 ps reported in the manuscript, we do not observe any significant signal decay at longer timescales up to 1 ns. This suggests that the signal intensity drop reported in Figure 3.3 is likely due to surface carrier diffusion, while the intrinsic carrier lifetime is significantly longer than 1 ns.

References

(1) Jena, S.; Tokas, R. B.; Thakur, S.; Udupa, D. V. PRISA: A User-Friendly Software for Determining Refractive Index, Extinction Co-Efficient, Dispersion Energy, Band Gap, and Thickness of Semiconductor and Dielectric Thin Films. *Nano Express* **2021**, *2*, 010008, DOI: `10.1088/2632-959X/abd967`.

(2) Géneaux, R.; Chang, H.-T.; Schwartzberg, A. M.; Marroux, H. J. B. Source Noise Suppression in Attosecond Transient Absorption Spectroscopy by Edge-Pixel Referencing. *Optics Express* **2021**, *29*, 951, DOI: `10.1364/OE.412117`.

(3) Silva, F.; Miranda, M.; Alonso, B.; Rauschenberger, J.; Pervak, V.; Crespo, H. Simultaneous Compression, Characterization and Phase Stabilization of GW-level 1.4 Cycle VIS-NIR Femtosecond Pulses Using a Single Dispersion-Scan Setup. *Optics Express* **2014**, *22*, 10181–10191, DOI: `10.1364/OE.22.010181`.

(4) Vinson, J.; Rehr, J. J.; Kas, J. J.; Shirley, E. L. Bethe-Salpeter Equation Calculations of Core Excitation Spectra. *Physical Review B* **2011**, *83*, 115106, DOI: `10.1103/PhysRevB.83.115106`.

(5) Gilmore, K.; Vinson, J.; Shirley, E. L.; Prendergast, D.; Pemmaraju, C. D.; Kas, J. J.; Vila, F. D.; Rehr, J. J. Efficient Implementation of Core-Excitation Bethe–Salpeter Equation Calculations. *Computer Physics Communications* **2015**, *197*, 109–117, DOI: `10.1016/j.cpc.2015.08.014`.

(6) Giannozzi, P. et al. QUANTUM ESPRESSO: A Modular and Open-Source Software Project for Quantum Simulations of Materials. *Journal of Physics: Condensed Matter* **2009**, *21*, 395502, DOI: `10.1088/0953-8984/21/39/395502`.

(7) Klein, I. M.; Liu, H.; Nimlos, D.; Krotz, A.; Cushing, S. K. *Ab Initio* Prediction of Excited-State and Polaron Effects in Transient XUV Measurements of α-Fe_2O_3. *Journal of the American Chemical Society* **2022**, *144*, 12834–12841, DOI: `10.1021/jacs.2c03994`.